ORIGINAL PAPER

Ultra-crystalline pyroclastic deposits and rhyolitic lavas controlled by crystal mushes: insights from the Acoculco Caldera Complex, México

Mario E. Boijseauneau-López[1] · **Giovanni Sosa-Ceballos**[2] · **Gabriela A. Farfán**[3] · **José Luis Macías**[2] · **Benjamin J. Andrews**[3]

Abstract

The Acoculco Caldera Complex (ACC), located in eastern Mexico, began its activity during the Pleistocene ~ 2.7 Ma. One of the most relevant and largest rhyolitic eruption in the complex, the Piedras Encimadas Ignimbrite (PEI), occurred during the late post-caldera phase at ~ 1.2 Ma. This ignimbrite is unique with respect to the other caldera products and other contemporaneous ignimbrites in the Trans-Mexican Volcanic Belt (TMVB) because of its ultra-high crystallinity and the absence of pumice fragments. The PEI is made almost entirely of crystals where the main constituents are k-feldspars and silica polymorphs that range from ≤ 5 μm to tens of centimeters in size. XRD on bulk rock, geochemical modeling, FTIR, Raman, and EPMA analyses were carried out in all mineral phases to assess the origin and the causes of high crystallinity within the PEI. We interpret the high crystallinity on the basis of magmatic crystallization of a magma body that was remobilized and altered by post-depositional hydrothermal alteration processes. We suggest that ACC rhyolites are geochemically influenced by at least one crystal mush established during the Pleistocene. We suggest that the PEI could be the result of an erupted crystal mush (melt + crystals), or a cumulate, or an ancient and crystallized reservoir generated after the first ACC collapse due to intrusion or underplating of mafic hot magmas. Extensional episodes within the ACC facilitated the ascent of mafic magmas. This interaction increased the liquid fraction of the mush through partial melting/crystal dissolution, generating a drop in density and viscosity in the mush, thus triggering eruption. The PEI provides evidences for an association between the geochemically-diverse ACC rhyolites with the complex interaction between mafic transitional alkaline magmas and a crustal mush system, promoted by continuous changes in the stress field during the Pleistocene.

Keywords Crystal-Mush · Acoculco Caldera Complex · Piedras Encimadas Ignimbrite · Trydimite · Cristobalite · Hydrothermal Alteration · Geothermal Exploration

✉ Mario E. Boijseauneau-López
cswasa@gmail.com

1 Posgrado en Ciencias de la Tierra, Escuela Nacional de Estudios Superiores, UNAM, Campus Morelia, 58190 Morelia Michoacán, México

2 Institute of Geophysics, UNAM, Campus Morelia, IGUM, 58190 Morelia Michoacán, Mexico

3 National Museum of Natural History, Smithsonian Institution, Washington D.C., USA

Introduction

The origin and evolution of rhyolitic magmas have been studied for decades (e.g. Whitney et al. 1989; Anderson et al. 2000; Bindeman and Valley 2003; Hildreth and Wilson 2007; Bindeman 2008; Scaillet et al. 2016; Jolles and Lange 2021; Clemens et al. 2022; Troch et al. 2022). Some of the largest (VEI > 6) ignimbrites are typically associated with rhyolitic magmas, but generation of its evolved magmas (regardless of the process, fractional crystallization or partial melting) involves segregation of melt-rich, crystal-poor magma from a crystal-rich source—the so-called crystal mush (Bachmann and Bergantz 2003, 2008a, b; Bachmann and Bergantz 2004a; Cashman et al. 2017). However, the depths of magma production,

extraction, final storage, and trigger mechanism of these eruptions remain controversial (Bachmann et al. 2002; Gottsmann et al. 2009; Malfait et al. 2014). It is widely accepted that the segregation of melt-rich forms aphyric rhyolitic magmas, crystal-poor magma from a crystal-rich source (Gualda et al. 2019). However, previous studies rarely have investigated if crystal-rich rhyolitic ignimbrites could be associated with the remobilization and reactivation of melt-dominant bodies that had cooled and crystallized close to the point of critical crystallinity or rheological lock-up at > ~ 50 vol.% of crystals (Marsh 1981; Brophy 1991; Vigneresse et al. 1996; Huber et al. 2010; Petford 2003); that is, the mobilization of a crystal mush including melt + crystals. Only, crystal-rich monotonous intermediates and aphyric rhyolitic ignimbrites have been stated as result of the activity of a crystal mushes (e.g., Hildreth 1981; Bachmann and Bergantz 2004a and 2008b; Hildreth and Wilson 2007; Blundy and Cashman 2008; Cashman and Giordano 2014; Zhang et al. 2018; Giordano and Caricchi 2022). Even more difficult to interpret are the cases of volcanic complexes with different ignimbrite types (crystal rich and crystal poor) and a series of rhyolitic lavas with no clear relationship to a crystal mush nor to a classical ignimbrite generation model. Crystal-rich, pumice-free ignimbrites with > 70 vol% crystals are sparsely described in the literature. This type of rhyolitic ignimbrites already has been interpreted as part of caldera eruptions related with a crystal mush; however, their origins are not fully understood (e.g., Sohn et al. 2009; Zhang et al. 2018).

The Acoculco Caldera Complex (ACC) in eastern Mexico (Fig. 1a) is an excellent case study because it hosts a great variety of rhyolites, comprising a syn-collapse ignimbrite, a series of annular rhyolitic domes (located in the rim of the caldera), and two post-collapse ignimbrites related to large eruptions triggered by local tectonics (Avellán et al. 2019, 2020). Furthermore, the ACC has pervasive hydrothermal alteration features distributed inside and outside the caldera, fumaroles, and hot spring waters. It is well documented how hydrothermalism generates alteration of the rocks in which the fluid circulation modifies the natural paragenesis and crystallinity through mineral chemical and structural modifications, as well as the precipitation of new mineral phases or the replacement of others (i.e., Schwartz 1959; Browne 1978; Giggenbach 1984; Kimball 1990; Mathieu 2018). The Piedras Encimadas Ignimbrite (PEI), the biggest felsic eruption reported in the ACC, is the first crystal-rich rhyolitic volcanic deposit described in Mexico. Due to its high crystal contents, we will examine if the hydrothermal alteration reported in the ACC changes the crystallinity or if the minerals are product of magmatic crystallization. Moreover, this study has broader applications for the understanding

of how crystal-rich deposits are produced and may help to determine the conditions in which a crystal mush model is applicable.

Here we characterize the geochemical, mineralogical, and trace element record of the PEI post-collapse ignimbrite and other felsic products of the ACC (Fig. 1b). We also propose a new model to understand the evolution of the ACC plumbing system and magmatism. This model links the different erupted compositions to a coherent differentiation scheme and is compatible with a process of crystal mush remobilization that controls the compositional variation within the ACC.

Geologic setting

The ACC is located on the eastern part of the Trans-Mexican Volcanic Belt (TMBV) (Fig. 1a). This volcanic arc is the product of the subduction of the Cocos and Rivera oceanic plates underneath the North American continental plate (Pardo and Suarez 1995; Gómez-Tuena et al. 2018). The local basement beneath the ACC region is formed by Cretaceous limestones (Avellán et al. 2019; López-Hernández et al. 2009), metamorphosed by a series of granitic intrusions of unknown age. Our knowledge of the local basement is the result of two exploratory wells performed by the Comisión Federal de Electricidad (CFE, the National Electricity Company). In addition to the metamorphic and sedimentary rocks, there are a series of aplitic dikes-sills (183 ± 36 ka, Avellán et al. 2019) and lava flows with basaltic andesitic and andesitic compositions (García-Palomo et al. 2018). Regional changes in stress orientations during the Miocene created a normal fault system with a NW–SE trend (García-Palomo et al. 2018; Gómez-Alvarez et al. 2021). This deformation in the southernmost part of the ACC zone developed to form the Tlaxco NW–SE fault system (Gómez-Alvarez et al. 2021). During the Pliocene–Pleistocene, the local stress changed, generating new normal fault systems in the Apan-Acoculco area with NW–SE orientations (García-Palomo et al. 2018). This structural system dominated until the late Pleistocene when the fault system orientation changed to NE–SW, producing graben-horst structures such as the Apan, Tlaxco-Chignauapan grabens, and the Rosario-Acoculco horst (García-Palomo et al. 2002, 2018).

Volcanic activity at the ACC started at 2.7 Ma and has been continuous until 0.016 Ma (Avellán et al. 2020). The volcanic evolution of the ACC was characterized by Avellán et al. (2019) into the categories syn-caldera, early post-caldera, late post-caldera, and extra-caldera units. The pre-caldera volcanism of the ACC comprises andesitic-dacitic domes; the syn-caldera stage generated the Acoculco andesitic ignimbrite (~ 2.7 Ma) and the first collapse of the region (Avellán et al. 2019). The collapse modified the local
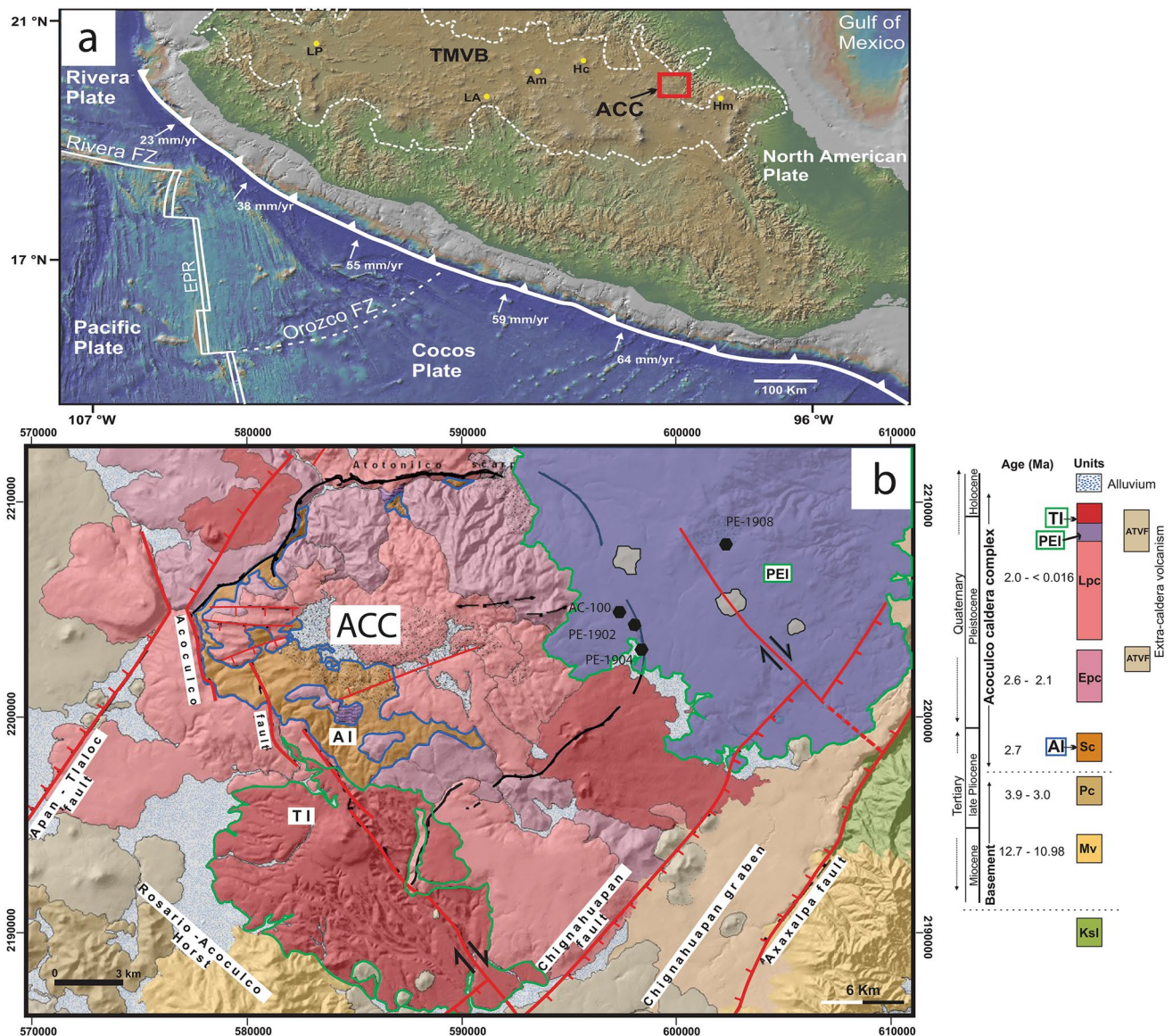
Fig. 1 a Location of the Acoculco Caldera Complex (ACC) within the Trans-Mexican Volcanic Belt (TMVB). **b** Simplified geological map of the ACC, after Sosa-Ceballos et al. (2018) and Avellán et al. (2019). The map contains the distribution of the basement rocks as limestones (Ksl), Peñuela and Quexnol (Mv), and the volcanic units; pre-caldera volcanism (Pc), syn-caldera volcanism (Sc), early post-caldera volcanism (Epc), late post-caldera volcanism (Lpc), and Extra-caldera volcanism (ATVF). The red lines represent the faults in the area after Calcagno et al. (2019) that form normal faults (NE–SW) and graben–horst structures. The localization of PEI samples is showed by a black mark on the map (modified from Pérez-Orózco et al. 2021)

stress field and promoted the ascent of peralkaline rhyolites mixed with calc-alkaline magmas (Sosa-Ceballos et al. 2018; Avellán et al. 2019). The post-caldera stage is characterized by bimodal volcanism: first with voluminous mafic rocks of the early post-caldera volcanism (2.6–2.2 Ma) followed by the late post-caldera volcanism (2–1 Ma), which comprised a series of rhyolitic domes, the PEI (Fig. 1b), Tecoloquillo ignimbrite (Avellán et al. 2020), and, finally, with a series of minor Quaternary monogenetic eruptions of mafic composition. The most voluminous episodes of rhyolitic volcanism

within the ACC area are represented by the PEI (Fig. 1b) and the Tecoloquillo ignimbrite. PEI is a welded ignimbrite with several flow units that appear as massive, light-gray to white, beds (Avellán et al. 2019, 2020). Each bed consists of microcrystalline matrix-supported particles with feldspar and quartz phenocrysts. It has an approximated volume of 26 km^3 (Avellán et al. 2020). The PEI represents caldera reactivation at 1.2 Ma, and its volcanic center was probably at the eastern portion of the ACC ring structure (López-Hernández et al. 2009; Avellán et al. 2020). The Later, another explosive

eruption occurred at ~ 0.8 Ma at the south part of the caldera producing the Tecoloquillo rhyolitic ignimbrite and its summit dome (Avellán et al. 2019). Pérez-Orozco et al. (2021) reveal that Tecoloquillo products show evidence of magma mixing between calc-alkaline and peralkaline melts. Furthermore, melt inclusions suggest that two magma bodies, located approximately 6–10 km in-depth and, isolated from one another, sourced the eruption (Pérez-Orozco et al. 2021). Older felsic products in the region are represented by the Peñuela Dacitic Dome Complex (~ 13–10 Ma) and Terrerillos Domes (~ 3 Ma) (García-Palomo et al. 2002; Avellán et al. 2019, 2020). It is not clear if magmatism is continuous between the Peñuelas and Terrerillos Dome complexes; however, felsic products are present in the late post-caldera units (~ 2–0.016 Ma) forming lava flows and domes with predominant rhyolitic compositions (Avellán et al. 2019, 2020). In addition, during the formation of the ACC, mafic volcanism (2.4–0.19 Ma) related to the Apan-Tezontepec Volcanic Field (ATVF) is interbedded with the products of the ACC and correspond to the extra-caldera stage (García-Palomo et al. 2002, 2018; López-Hernández et al. 2009; Avellán et al. 2019).

The interest in exploring the ACC region arose in the 1980s with prospective works carried out by the Mexican Federal Electricity Commission (CFE, for its acronym in Spanish) to determine its geothermal potential. Despite the hydrothermal alteration being the most outstanding feature of most ACC deposits (Canet et al. 2015), there are few spots of superficial geothermal manifestations such as springs and fumaroles (Lopez-Hernandez and Castillo-Hernandez 1997). The alteration features are reported for an area of several square km in the center of the caldera complex, and outside, in the eastern border, affecting pyroclastic deposits, and, to a lesser degree, lavas (Canet et al. 2015; Sánchez-Córdova et al. 2020; Pandarinath et al. 2020). Inside the caldera, the most common hydrothermal alteration is the silicic type. There are some regions where acid-sulfate alteration types can be found (vuggy silica and advanced argillic alterations); however, outside of the caldera, the hydrothermal alteration has no studies.

Methods

We collected bulk rock samples (comprising crystals and matrix) from the bottom, middle, and top portions. We study four sections of the PEI in proximal and distant deposits in gullies of the western caldera borders (Fig. 1b). The field strategy consisted of sampling the deposit based on vertical variations. Samples were crushed and hand-picked to obtain lithic-free fragments for analysis. Whole-rock analysis of major and trace element concentrations were determined by fusion inductively coupled plasma emission spectroscopy

(ICP-ES) and inductively coupled plasma mass spectrometry (ICP-MS) at the Activation Laboratories, Ancaster, Canada (https://actlabs.com/). Fifteen rock samples were cut and processed into thin polished sections for petrographic and electron microprobe analysis (EPMA).

To investigate how hydrothermal alteration could modify the crystallinity of the PEI deposits, Fourier-transform infrared spectroscopy (FTIR), Raman spectroscopy, and X-ray diffraction (XRD) were carried out on mineral samples and on the matrix of different samples. On each sample (bottom, middle top), we realize 1 XRD analysis, more than 35 FTIR analysis and more than 30 Raman analysis per each thin section. FTIR analyses were performed with a Thermo Scientific apparatus at the Laboratorio de Microanálisis, CEMIE-Geo UNAM. Micro-FTIR analyses were measured with 512 scans at a resolution of 4 cm^{-1} and were collected using a KBr beam splitter. The sample was placed on a water-free KBr base for support, and the background scan and sample analyses were taken through the KBr base under the same analytical conditions. Micro-FTIR analyses were obtained over a wavelength range of 5000–600 cm^{-1}, with a liquid-nitrogen cooled HgCdTe2 (MCT) detector and an aperture set at 10 µm square. This provided a strong intensity and detector response for the mid-IR water absorbance bands. Raman analyses were performed with a Thermo Scientific DXR apparatus at the Laboratorio de Microanálisis, CEMIE-Geo UNAM. Raman measurements were carried out in the matrix and minerals of all the PEI deposits. Raman analyses were measured with a 532 nm laser over a wavelength range of 3568–20 cm^{-1}, at a resolution of 1.7–2.7 cm^{-1}, with a 50 µm aperture and 8.8 mV of laser power.

Mineral compositions were determined for a representative subset of the PEI samples. Major-element compositions of plagioclase and Fe-Ti oxides were acquired using a JEOL JXA-8230 electron microprobe housed at the Laboratorio de Microanálisis, CEMIE-Geo UNAM. Analytical conditions were 15 keV accelerating voltage and 10 nA current for major elements and 15 keV and 20 nA for selected trace elements; a focused beam was used in both cases. A defocused electron beam of 10 µm was used to analyze glass groundmass to avoid Na migration. Analytic uncertainties in EPMA were determined with secondary standards with a variety of minerals and glasses. Standards were analyzed throughout each analytical session to monitor instrument drift and correct compositional offsets.

Mineral phase identification was achieved using powder X-ray diffraction (XRD) on a Rigaku D/MAX-Rapid micro-X-ray diffractometer at the Smithsonian National Museum of Natural History Department of Mineral Sciences, EUA. The instrument uses Mo Kα radiation (λ = 0.71069 Å) and collects data on a 2D imaging plate detector with Debye–Scherrer geometry. Sample powders were gently re-ground in an agate mortar and pestle and were mounted in 1 µm-wide

Kapton capillaries. The samples were run for 10 min each with omega fixed at 0° and phi rotating at 1°/second. Three sample replicates were collected for each sample by focusing the X-ray beam on three different regions of the powder-filled capillary. XRD image files were background-corrected (manual setting = 4) and integrated into intensity vs 2θ patterns from 4.0 to 45.0 2θ degrees and 81.6337–430.00 β using 2DP software.

Mineral phases in our samples were initially identified using the search/match function of Jade (2021) (Materials Data, Inc.) with the PDF-4 2021 ICDD database. Contributions of mineral phases in each of the different samples (represented as phase percentages and weight percentages) were estimated via whole pattern Rietveld refinement analyses using GSASII software (Toby and Von Dreele 2013; Post and Bish 1989). The background was modeled using a Chebyschev polynomial. Anorthoclase [(Al, Si$_3$) (Na$_{0.667}$K$_{0.333}$) O$_8$; Harlow 1982], quartz (Antao et al. 2008), cristobalite (Downs and Palmer 1994), tridymite with a monoclinic structure (Hirose et al. 2005), and tridymite with an orthorhombic structure (Lee and Xu 2019) were used as model structures. Although there are likely other feldspar phases present, our focus was to identify and quantify the tridymite and cristobalite phases in these samples. We selected anorthoclase as a single representative feldspar in this system to minimize the number of phases in the Rietveld refinement. Errors in phase estimates represent standard deviations in measurements between the three replicates.

Given the mush-like nature of the PEI deposits, we tested with a geochemical model (Fig. 13) if rhyolites have a relationship with melt extracts produced in a crystal mush, probably peralkaline in composition, or if these rocks are not affected by the crystal mush. We chose to perform partial melt models because most authors, regardless of the tectonic context in which volcanism occurs, show that partial melt episodes can occur in the cumulate part of crystal mushes (Foley et al. 2020 and cites therein). This can be promoted by the flow of volatiles and heat coming, in general, from some mafic-intrusive melts in the base of the cumulate portion of the mush (Bachmann et al. 2002; Deering et al. 2011; Foley et al. 2020; Lubbers et al. 2020; Pamukcu et al. 2013; Sliwinski et al. 2017; Szymanowski et al. 2017; Tavazzani et al. 2020). The process above described eventually triggers the mobilization of the crystal mush.

For the model, we assume the following: (i) the mush extracts behave like a partial melt, (ii) PEI deposits represent the eruption of a portion of a crystal mush (partial melts + crystals), (iii) we use different granitic rock compositions for the model because a crystal mush can spawn from the crystallization of a magma body or by the partial melting of a pre-existing crystallized body in any tectonic setting. However, we choose the chemical composition of a xenolith of an intrusive granitic rock reported by

Sosa-Ceballos et al. (2018) and PEI as a proxy of the partial melting source that produce the melt extracts; (iv) the injection of hot mafic magma promotes the partial melting but lead to produce a minimal chemical interaction with the mush and unevenly distributed thermal flux (Foley et al. 2020); (v) we consider the multiple crystal mush scenario, hosted in different portions of the upper crust. Due to the geochemical modeling complexity, we decided to explore partial melting as a process that could occur in one crystal mush. To run the model, we consider the partial melting of the granitic proxy in a range of F = 0.05–0.45 (5–45%) for the xenolith sample, F = 0.1–1(0.1,0.15,0.2, …,1) for the PEI sample; we used a paragenesis of 0.45 K-Fls + 0.35 Plg + 0.10 Qz + 0.05Opx + 0.05Cpx for the xenolith sample and 0.45 K-Fls + 0.35 Qz + 0.10 Plg + 0.05Opx + 0.05Cpx for the PEI model. We used distribution coefficients of some REE, Rb and Zr in mineral phases published by Rollinson (2014) with the equation Cl = C0/ (F + (D(1-F)).

Results

The PEI deposits, like most of the ACC rhyolitic deposits, are dispersed in the outer zone of the caldera (Fig. 1b). The PEI is massive, gray white, and crystal rich (Fig. 2). The maximum observed thickness is ~ 100 m, and deposits are generally welded at the bottom and more friable toward the top (Fig. 2b, c). The contact between the local basement and the base of the deposit, or the lag breccia, does not crop out around the ACC, although Avellán et al. (2019) and López-Hernández et al. (2009) suggest that the eastern border of the caldera was the emission point of the PEI. The deposits are composed almost entirely of microphenocrysts and phenocrysts (~ 1% vol of crystal with sizes > 15 cm) of alkali feldspar, quartz, plagioclase, and Fe-Ti oxides (Fig. 3 a, b, c, d) with a crystal content up to ~ 90 wt. % in welded portions and ~ 60 wt. % in friable deposits (Fig. 3). Neither pumice, glass chips, nor lithic fragments are found within the deposits. Portions of the deposit appear to contain an ashy matrix (Fig. 2 d), but the matrix comprises aggregates of quartz and feldspar with sizes > 5 μm, as observed in the welded portion (Fig. 3). The friable portion of the PEI has portions with argillic hydrothermal alteration (Fig. 2a). This alteration was reported by Canet et al. (2015) in the inner part of the caldera.

The PEI is rhyolitic in bulk rock composition and has slight internal vertical chemical variations (Fig. 4, Table 1) The compositions of the PEI sample become more silicic and exhibit a decrease in Fe$_2$O$_3$ and MgO toward the top of the deposit. We analyzed unaltered samples with LOI values below 1 wt. %. Trace element concentrations normalized to the primitive mantle (Sun and McDonough 1989) show negative anomalies of Ba, Nb, Ta, U, Th, K, and Zr,

Fig. 2 Photographs showing the PEI field features of the deposit: **a** The non-welded top of the deposit, **b** The welded middle part of the deposit, **c** welded bottom part of the deposit, and **d** a cm-scale feldspar phenocryst
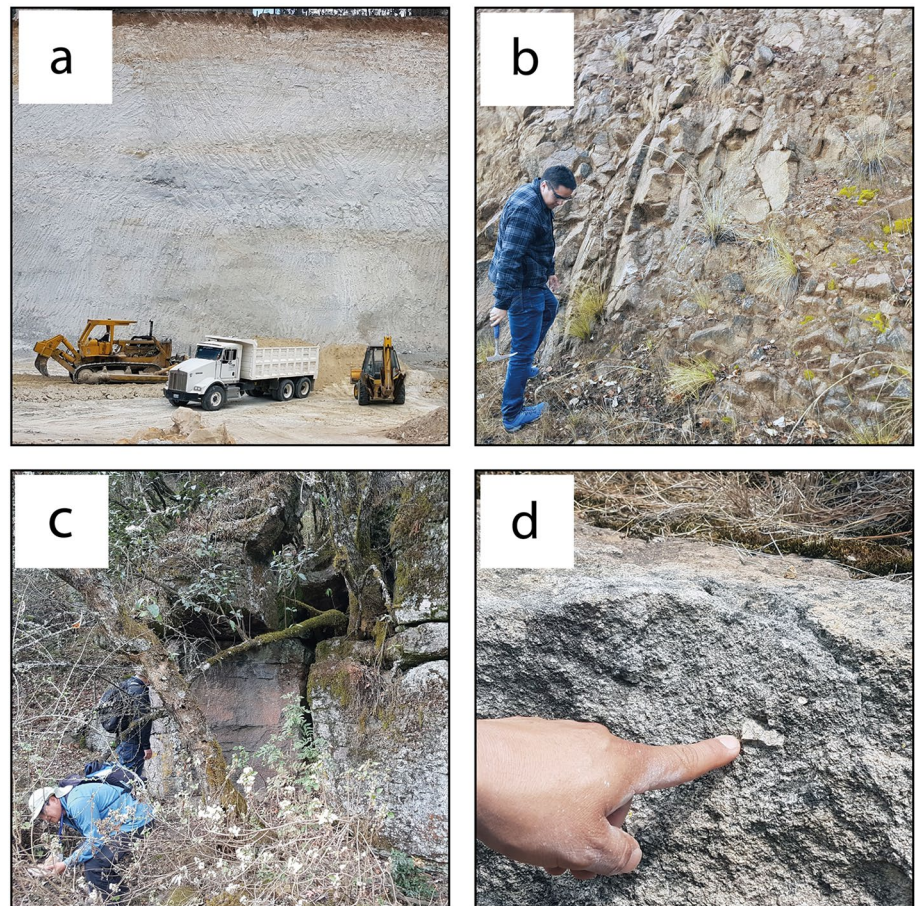

and a positive anomaly of Pb, Sr, Eu, P, and Ti. Furthermore, heavy rare earth elements (HREE) present a horizontal trend and light rare earth elements (LREE) are more enriched than HREE (Fig. 5). These anomalies and trace element concentrations are also present in the other felsic members of ACC such as Tecoloquillo ignimbrite (TQ) and xenolith fragments of granitic composition reported by Sosa-Ceballos et al. (2018). The xenolith fragment may come from felsic intrusions associated with the ACC magmatic system. Felsic intrusions are reported by CFE exploratory drilling in the region, where they are described as aplitic dikes. ACC's pyroclastic and lava felsic products show low $Eu/Eu^* \leq 0.3$ and low Ba < 500 ppm (Fig. 6b, e). Moreover, these rocks show a positive trend in Ba/Rb vs Rb, Rb vs La, low #MgO (1–16), and a wide range in the La/Sm vs La diagrams (Fig. 6d). The composition of rhyolites in the ACC is diverse but can be distinguished between A-type and calc-alkaline I-Type rhyolites as a result of the analysis of $Zr + Nb + Y + Ce$ and trace elements (Fig. 6a). Calc-alkaline rhyolites tend to have higher Ba/Sr and lower La/Yb ratios and higher abundances of HFSE and HREE than A-type rhyolites (Fig. 6a).

The larger phenocrysts of feldspar are average 1 cm in size (but can exceed 15 cm in length; Fig. 2d) and have

subhedral broken shapes (Fig. 3a). Microphenocrysts and phenocrysts show disequilibrium features such as exsolution textures, rounded borders, and resorbed rims (Fig. 3c, d). Furthermore, all the PEI deposits show relics of mafic minerals. Feldspar phenocrysts have anorthoclase and sanidine compositions with 2–8 mol% An and 20–78 mol% Or, whereas the matrix is formed by orthoclase and microcline (Fig. 9). XRD and Raman analyses, however, show that phenocrysts in the samples have an anorthoclase structure (Figs. 10, 11). Oxides in the PEI deposits are ferropseudobrookite–ilmenite and ulvospinel–wustite. Furthermore, oxides display variations of FeO, Fe_2O_3, and TiO_2 from the center to the rim of the phenocrysts (Supplementary material). Core to rim transects in oxides show Fe enrichment with Ti depletion (Fig. 8).

The composition of the PEI matrix samples exhibits a mixture of quartz and felspar (Fig. 10a). EPMA imaging and compositional analysis of the PEI samples reveals that the matrix is composed of microcrystalline texture (< 5 µm) of quartz and feldspar with, 6–13 wt. % of $Na_2O + K_2O$ (Fig. 7, 8, 9). FTIR spectroscopy shows primarily anorthoclase and quartz crystals with no hydroxy or water structural defects in the 3000–3800 cm^{-1} bands.
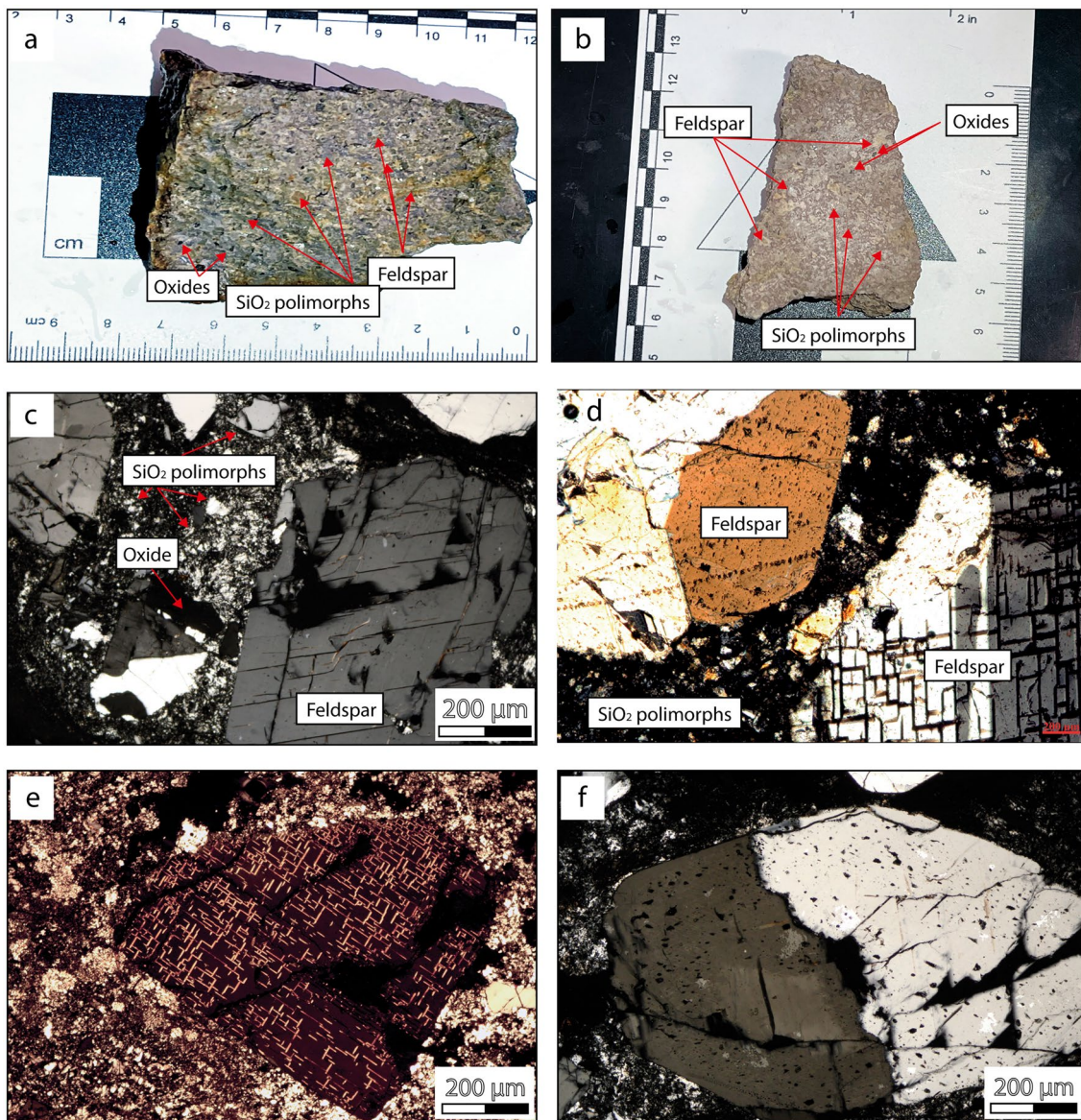
Fig. 3 Photomicrographs of four PEI samples in cross-polarized light. **a** The mineral assemblage formed by phenocrysts of feldspar and quartz and a groundmass formed by tridymite and cristobalite crystals; **b** The few plagioclase phenocrysts often have disequilibrium textures, such as rounded borders and sieve texture; **c** a feldspar phenocryst with exsolution texture and rounded borders; **d** a feldspar phenocryst with rounded borders and twining

Rietveld refinements of X-ray diffraction patterns (Fig. 10a) estimate the relative contribution of different mineral phases outlined in Table 2. Anorthoclase and quartz dominate, as expected, with smaller contributions of cristobalite and tridymite as monoclinic and orthorhombic phases. Cristobalite is not present in PE1904. Orthorhombic tridymite is present in sample AC100. Due to the absence of clay minerals and glass in the XRD patterns, we use the results of Rietveld refinements as a proxy of %vol for each sample (Table 2).

Discussion

Matrix-free deposits: a hydrothermal fingerprint

The PEI deposits contain microcrysts of quartz, cristobalite, and tridymite as confirmed in FTIR and Raman analysis (Fig. 11a, b). Likewise, XRD measurements show crystal structures of polymorphs of silica (Fig. 10). These mineral phases are related to hydrothermal alteration and
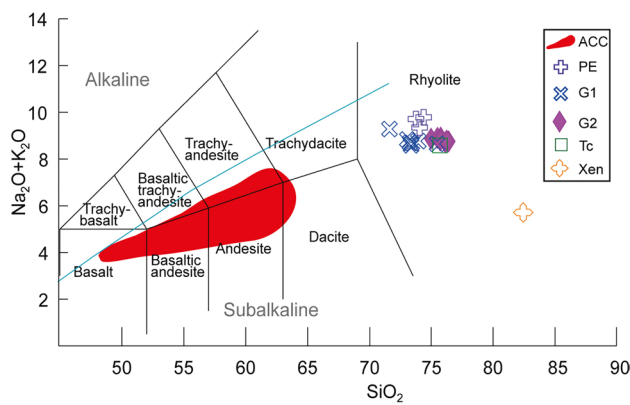
Fig. 4 Total alkali vs silica diagram of the Acoculco Caldera Complex (ACC, red field) rocks, PE = Piedras Encimadas Ignimbrite simples, Tc = Tecoloquillo ignimbrite, Xen = xenolith, blue cross symbols represent G1, and diamond symbols represents G2 rhyolite ACC lavas of the early and late post-caldera events

are reported in other deposits in the inner portion of the ACC (Canet et al. 2015; Sánchez-Córdova et al. 2020). In the less crystalline portions of the PEI, the content of quartz, cristobalite, and tridymite aggregates can reach 40–50 vol% in the welded portions at the bottom part of the deposit. Additionally, to the top of the deposit, crystals are supported by a cryptocrystalline matrix formed by silica polymorphs (Fig. 2a). Thus, we suggest that late hydrothermal alteration affected the deposits even in the external parts of the caldera. Syn- and post-depositional alteration of primary volcanic deposits with the formation of clay minerals have been observed in pyroclastic surge deposits, e.g., at Vulcano, Italy (Capaccioni and Coniglio 1995) and El Chichón, México (Macías et al. 1997). However, we do not have clay minerals. This evidence could suggest that the matrix-free nature of the welded portion of the PEI deposits could be produced by hydrothermal alteration.

One of the pending questions to be resolved is how the SiO_2 polymorphs of the PEI were formed and in which pressure and temperature conditions. Cristobalite and tridymite crystals commonly precipitate at low pressures up to ~0.4 GPa and temperatures between 870 °C and 1470 °C, but these minerals also exist as metastable phases at lower temperature conditions (Kihara et al. 1986; Heaney et al. 1994); Deer et al. 2004). Tridymite crystals tend to exhibit a hexagonal structure above ~ 380 °C with slight distortions of the Si–O–Si bond angles and Si–O bond length (Kihara et al. 1986). Between 380 °C and 110 °C, tridymite recrystallizes to form an orthorhombic structure, and below 110 °C, monoclinic tridymite is ubiquitous (Heaney et al. 1994). All the PEI deposits contain sharp, well-defined XRD peaks of monoclinic (Fig. 10) tridymite and cristobalite. However, orthorhombic

tridymite is only clearly present in samples AC100 and PE-1902 (Fig. 11). AC100 is located in the SW border of ACC near the topographic rim described by Sosa-Ceballos et al. (2018). Therefore, orthorhombic tridymite found in the PEI deposits could suggest that hydrothermal fluids circulated and reached temperatures up to 110 °C and that these fluids promoted the devitrification process of the deposits. Furthermore, the wüstite composition of the Fe-Ti oxides (Fig. 8) suggest hydrothermal alteration process. Wüstite minerals are reported in hydrothermal veins formed in low fugacity conditions or during the exsolution of pre-existing oxides (Nadoll and Mauk 2011), as observed in S-type granites where the exsolution of oxides should occur during the partial melting of metapelitic rocks (Seifert et al. 2010).

The devitrification of rhyolitic pyroclastic rocks is a relatively common process, resulting in the production of microcrystalline silica and feldspars from the fast emplaced and slow cooling deposits (Rowe et al. 2012) and by post-depositional hydrothermal circulation. These chemical alteration processes lead to mass fluxes of elements, both from the altered glass into solution and vice versa, as it has been also reported in mafic rocks from the ocean floor (Furnes 1978); Zhou and Fyfe 1989; Crovisier et al. 1992; Stroncik and Schmincke 2001; Walton et al. 2003; Pauly et al. 2011). In ACC, this process was studied and quantified by Sánchez-Córdova et al. (2020). As a result of the hydrothermal alteration process, the supersaturation of fluids causes the precipitation of neoformation minerals (Hay and Iijima 1968; Ibrahim and Hall 1996; Stroncik and Schmincke 2001; Kousehlar et al. 2012) such as the tridymite and cristobalite observed in the PEI samples (Fig. 7a). Furthermore, the silicification was well-studied in the central ACC (Sánchez-Córdova et al. 2020). The alteration processes are, thus, pervasive and likely affect the matrix to a greater degree because of the devitrification process after emplacement of the pyroclastic density currents. Feldspars do not show signs of alteration such as albitization (despite of low %Or), a distinct reddening, relics of its ancient feldspar/plagioclase compositions and/or the absence of micrometric/nanometric pores containing white mica (Engvik et al. 2008), alteration to sericite, zeolites, or other typical alteration minerals (Figs. 10, 11). Thus, the pre-existing ash matrix of the PEI could be transformed to tridymite + cristobalite + K-feldspars (Rowe et al. 2012), as it was observed in the XRD, Raman, FTIR, and EPMA maps (Fig. 7, 10, 11). If this is true, the hypothetical glass (pumice fragments) or matrix (formed by fine ash particles) content could reach less than 40% vol of deposits, as is observed in petrography and quantified by Rietveld refinement of XRD patterns (Table 2). Thus, given the pervasive hydrothermal alteration described in the ACC, we propose the matrix was replaced by secondary minerals. Such replacement processes have been described in other

Table 1 Major and trace geochemistry of ACC samples. Error for major elements is ~0.01 wt% and trace elements ~1 ppm in average

Units	Ec	Lpc	Lpc	Lpc	Ec	Epc	Lpc	Lpc	Lpc	Lpc	Lpc	Lpc	Lpc	Lpc	Lpc	Lpc	Lpc	Lpc	Epc
Sample	TQ-Ac12	PEI-Ac100	PEI-1902	PEI-1904	Ac7	Ac90	Ac107	Ac108	Ac113	Ac115	Ac35	Ac37	Ac51	Ac56	Ac72	Ac82	Ac89	Ac92	Ac112
Age Ma	611±72	1278±14	1278±14	1278±14		2553±110	1438±24		1870±36	1300±600	1700±400	1084±22	1600±100	1400±200	1283±88	1145±14	1066±42	1360±15	
Age (Ma)	611	1278	1278	1278		2553	1438		1870	1300	1700	1084	1600	1400	1283	1145	1066	1360	
East	586,067	596,510	599,601	597,037	582,915	574,826	590,387	588,634	584,295	589,651	576,764	575,914	588,654	581,401	578,889	595,629	572,356	583,057	584,862
North	2,192,035	2,204,497	2,204,605	2,203,900	2,194,317	2,208,919	2,213,875	2,212,926	2,196,999	2,210,789	2,200,734	2,199,284	2,205,382	2,204,474	2,199,502	2,190,307	2,208,434	2,213,879	2,197,201
Type	Pyroclast	Pyroclast	Pyroclast	Pyroclast	Lava	Lava	Lava	Lava	Lava	Lava	Lava	Pyroclast	Lava	Lava	Lava	Lava	Lava	Lava	Xen
SiO2	76.91	74.15	72.86	73.99	73.2	76.62	71.98	76.27	75.88	72.7	71.13	75.08	70.04	73.01	74.7	74.71	72.19	75.36	83.11
Al2O3	12.53	13.73	14.46	13.38	12.56	11.86	13.81	12.86	11.96	13.58	13.21	11.55	14.88	14.22	12.58	11.46	13.24	12.99	8.02
Fe2O3(T)	1.78	0.97	0.92	2.15	1.61	1.78	2.1	1.34	2.14	2.25	2.21	1.43	2.53	1.58	1.26	1.72	2.92	1.44	1.22
Fe2O3	0.18	0.10	0.09	0.22	0.16	0.18	0.21	0.13	0.21	0.23	0.22	0.14	0.25	0.16	0.13	0.17	0.29	0.14	0.12
FeO	1.60	0.87	0.83	1.93	1.45	1.60	1.89	1.21	1.93	2.02	1.99	1.29	2.28	1.42	1.13	1.55	2.63	1.30	1.10
MnO	0.04	0.013	0.01	0.017	0.042	0.049	0.059	0.052	0.039	0.09	0.076	0.046	0.038	0.028	0.048	0.048	0.045	0.051	0.023
MgO	0.11	0.03	0.02	0.03	0.12	0.08	0.24	0.09	0.05	0.29	0.38	0.07	0.12	0.04	0.04	0.05	0.08	0.08	0.09
CaO	0.44	0.19	0.22	0.23	0.55	0.38	0.67	0.41	0.08	0.95	1.04	0.36	0.66	0.47	0.34	0.31	0.56	0.3	0.3
Na2O	3.92	4.6	4.49	4.34	3.48	3.69	3.98	3.92	4.19	4.24	4.03	2.87	4.73	4.01	3.2	3.32	4.04	3.67	2.52
K2O	4.78	5.19	5.15	5.04	5.18	5.06	4.56	5.07	4.73	4.42	4.62	5.71	4.44	4.67	5.46	5.27	4.44	4.96	3.09
TiO2	0.179	0.23	0.245	0.227	0.178	0.135	0.337	0.178	0.21	0.355	0.362	0.139	0.471	0.24	0.143	0.135	0.385	0.182	0.126
P2O5	0.02	0.03		0.05	0.02	0.01				0.07	0.07	0.01	0.05	0.02	0.01		0.22	0.02	0.01
LOI	0.25	0.26	0.82	0.91	2.83	0.51	1.14	0.62	0.48	0.37	2.97	3.58	1.18	1.44	2.82	3.67	1.93	0.67	1.14
Total	101	99.4	99.21	100.4	99.76	100.2	98.86	100.8	99.77	99.32	100.1	100.9	99.15	99.72	100.6	100.7	100.1	99.72	99.66
#MgO	6	3	2	1	7	4	11	6	2	12	16	5	5	2	3	3	3	5	7
Sc	2	2	4	5	3	3	4	3	5	4	4	3	6	3	2	3	5	2	2
Be	6	5	4	5	7	6	4	6	5	5	5	6	4	3	6	7	5	5	4
V	6		9	6	6		12	5		12	12		11	6			19		6
Cr	30									70								20	
Co	1				38	27	12	22	31	1	18	2	7	6	14	1	22		54
Ni	5	3	1		2	1	2		2		3	4	2	2	2	3	2	2	2
Cu	7	4	2	2	6	3					7	10	3	2	2	5	4	3	<1
Zn	55	21	18	54	56	49	46	53	73	60	69	52	72	46	51	60	58	47	42
S	40	20	0.006	0.029	20	40	60	60	50	30	40	20	30	20	20	20	40	30	30
Ga	24	22	22	20	22	20	22	21	22	22	21	21	24	20	21	21	22	21	15
Ge	2.3	1.8	1.4	1.6	1.9	2.2	1.7	1.8	1.9	1.8	1.7	2.2	1.8	1.6	2	2.1	1.5	1.9	1.2
As	18	<5			14	13	6	9	6	7	7	13		6	11	15	7	9	
Rb	207	128	118	126	202	164	143	162	171	133	138	174	121	150	164	165	145	151	136
Sr	30	15	17	17	27	8	75	21	2	91	88	7	122	52	11	4	74	21	19
Y	47.4	37.3	34.9	40.4	60.7	42.7	27	51.1	52.6	43.1	40.5	44.6	42.6	27.2	44.6	53.4	87.9	54.9	38.6
Zr	181	439	425	403	232	160	302	196	500	324	324	185	499	227	168	271	446	181	136
Nb	31.3	29.8	35.5	36.8	30.7	29.2	26.4	28.3	31.9	26.8	27.5	30.7	33.1	18.5	25.4	34.3	28.5	27.2	20.4
Mo	7	3	2	2	7	8	4	7	2	4	7	9	4	4	7	9	5	3	
Sn	2	3	3	4	6	5	2	4	4	3	3	6	3	3	4	6	3	3	
Sb	2.1	0.8	0.8	1	1.2	1.2	0.5	0.8	0.5	0.9	0.6	1.3	0.4	0.6	0.7	1.3	0.2	1	0.2
Cs	11.8	2.5	1.4	1.8	6.2	5.1	2.3	4.1	2.7	3.9	3.9	5.1	1.3	3.5	4.4	5.2	2.5	3.4	3.1

Table 1 (continued)

Units	Ec	Lpc	Lpc	Lpc	Ec	Epc	Lpc	Lpc	Lpc	Lpc	Lpc	Lpc	Lpc	Lpc	Lpc	Lpc	Lpc	Lpc	Epc
Sample	TQ-Ac12	PEI-Ac100	PEI-1902	PEI-1904	Ac7	Ac90	Ac107	Ac108	Ac113	Ac115	Ac35	Ac37	Ac51	Ac56	Ac72	Ac82	Ac89	Ac92	Ac112
Ba	133	163	200	152	131	74	430	233	39	503	457	67	632	611	134	22	302	212	85
La	65.3	52	35.8	52.8	64.1	58.3	37.7	62	66.7	54.5	48.9	59.2	51.1	50.9	63.8	67	89.9	61.8	42.6
Ce	125	108	68.7	100	121	110	89.5	110	116	125	98.3	112	110	62.1	112	124	119	101	83.7
Pr	13.6	11.4	8.07	12.2	13.3	11.8	7.41	12.3	14.8	12.1	10.4	12.6	11.9	9.86	13.2	14.8	19	14	8.69
Nd	45	40.3	28.5	43.2	45.5	40.7	25.8	43.4	52.3	42.3	37.3	41.9	42.3	32.8	44.7	51.5	70.2	49.2	29.5
Sm	8.12	7.6	5.8	8.29	8.8	7.51	5.06	8.47	9.83	8.22	7.17	8.04	8.98	5.61	8.49	9.69	13.9	9.54	5.91
Eu	0.374	0.44	0.543	0.434	0.352	0.229	1.02	0.642	0.375	1.2	1.14	0.248	2.22	0.761	0.327	0.186	0.855	0.608	0.238
Gd	6.1	5.82	4.88	6.82	8.37	5.73	4.25	7.51	8.91	7.12	6.59	6.43	7.79	4.68	7.45	7.34	13.7	7.52	5.3
Tb	1.2	1.03	0.85	1.14	1.5	1.08	0.75	1.27	1.56	1.16	1.08	1.15	1.36	0.81	1.26	1.35	2.29	1.35	0.92
Dy	7.55	6.43	5.48	7.14	9.72	6.71	4.71	8.4	9.9	7.16	6.99	7.02	8.11	5.05	7.77	8.57	14.3	8.03	6.04
Ho	1.59	1.35	1.12	1.44	1.98	1.39	0.89	1.63	1.87	1.46	1.36	1.42	1.5	0.92	1.55	1.7	2.81	1.63	1.26
Er	4.89	3.97	3.49	4.09	6.25	4.2	2.94	5.06	5.8	4.42	4.2	4.34	4.64	2.88	4.82	5.23	8.49	5.06	3.91
Tm	0.845	0.69	0.585	0.643	0.991	0.738	0.475	0.795	0.874	0.694	0.645	0.748	0.69	0.452	0.7	0.895	1.27	0.849	0.61
Yb	5.59	4.59	3.95	4.39	6.7	4.88	3.21	5.17	6.29	4.66	4.76	5.12	4.83	3.16	5.21	6.04	8.75	5.63	4.39
Lu	0.79	0.66	0.655	0.726	1.02	0.69	0.507	0.797	0.956	0.717	0.674	0.732	0.721	0.437	0.735	0.856	1.35	0.852	0.674
Hf	5.5	9.3	10.7	9.8	7.1	5	7.7	6.1	12.5	7.9	8.6	5.5	11.7	6.1	5.5	7.6	10.3	5.1	4.7
Ta	3.39	2.49	2.54	2.63	3.89	3.21	3	3.25	3.37	2.9	2.78	3	2.77	2.08	3.16	3.37	3.01	2.81	2.7
W	3.5	2.1	1.1	1.2	373	252	84	233	254	12.1	156	2.9	58.3	38.7	122	2.7	196	5.4	489
Tl	0.37	0.33	0.27	0.36	1.23	0.72	0.97	0.91	0.71	0.63	0.89	0.8	0.39	0.57	1.2	0.88	0.68	0.51	0.22
Pb	16	16	14	16	17	15	17	14	25	17	16	12	15	16	17	15	12	13	10
Th	19.1	13.2	13.9	14	20.8	16.4	16.1	16.3	16.3	14.8	14.2	16.3	11.7	13.4	17.7	17	14.8	15.3	12.7
U	6.23	4.42	3.92	4.01	6.09	5.51	4.48	4.79	4.81	4.81	4.2	5.26	3.54	3.85	4.84	5.55	5.21	4.99	6.41
Eu*	7.18	6.77	5.36	7.59	8.59	6.68	4.67	8.00	9.38	7.69	6.89	7.28	8.41	5.17	7.99	8.60	13.80	8.59	5.61
Ba/Rb	0.64	1.27	1.69	1.21	0.65	0.45	3.01	1.44	0.23	3.78	3.31	0.39	5.22	4.07	0.82	0.13	2.08	1.40	0.63
Nb/Th	1.6387	2.2576	2.5540	2.6286	1.4760	1.7805	1.6398	1.7362	1.9571	1.8108	1.9366	1.8834	2.8291	1.3806	1.4350	2.0176	1.9257	1.7778	1.6063
Ta/U	0.5441	0.5633	0.6480	0.6559	0.6388	0.5826	0.6696	0.6785	0.7006	0.6029	0.6619	0.5703	0.7825	0.5403	0.6529	0.6072	0.5777	0.5631	0.4212
Nb*	0.1931	0.2660	0.3009	0.3097	0.1739	0.2098	0.1932	0.2045	0.2306	0.2133	0.2282	0.2219	0.3333	0.1627	0.1691	0.2377	0.2269	0.2094	0.1892
Ta*	0.2787	0.2885	0.3319	0.3359	0.3272	0.2984	0.3430	0.3475	0.3589	0.3088	0.3390	0.2921	0.4008	0.2767	0.3344	0.3110	0.2959	0.2884	0.2157
Nb/Th PM	8.4881	8.4881	8.4881	8.4881	8.4881	8.4881	8.4881	8.4881	8.4881	8.4881	8.4881	8.4881	8.4881	8.4881	8.4881	8.4881	8.4881	8.4881	8.4881
Ta/U PM	1.9524	1.9524	1.9524	1.9524	1.9524	1.9524	1.9524	1.9524	1.9524	1.9524	1.9524	1.9524	1.9524	1.9524	1.9524	1.9524	1.9524	1.9524	1.9524
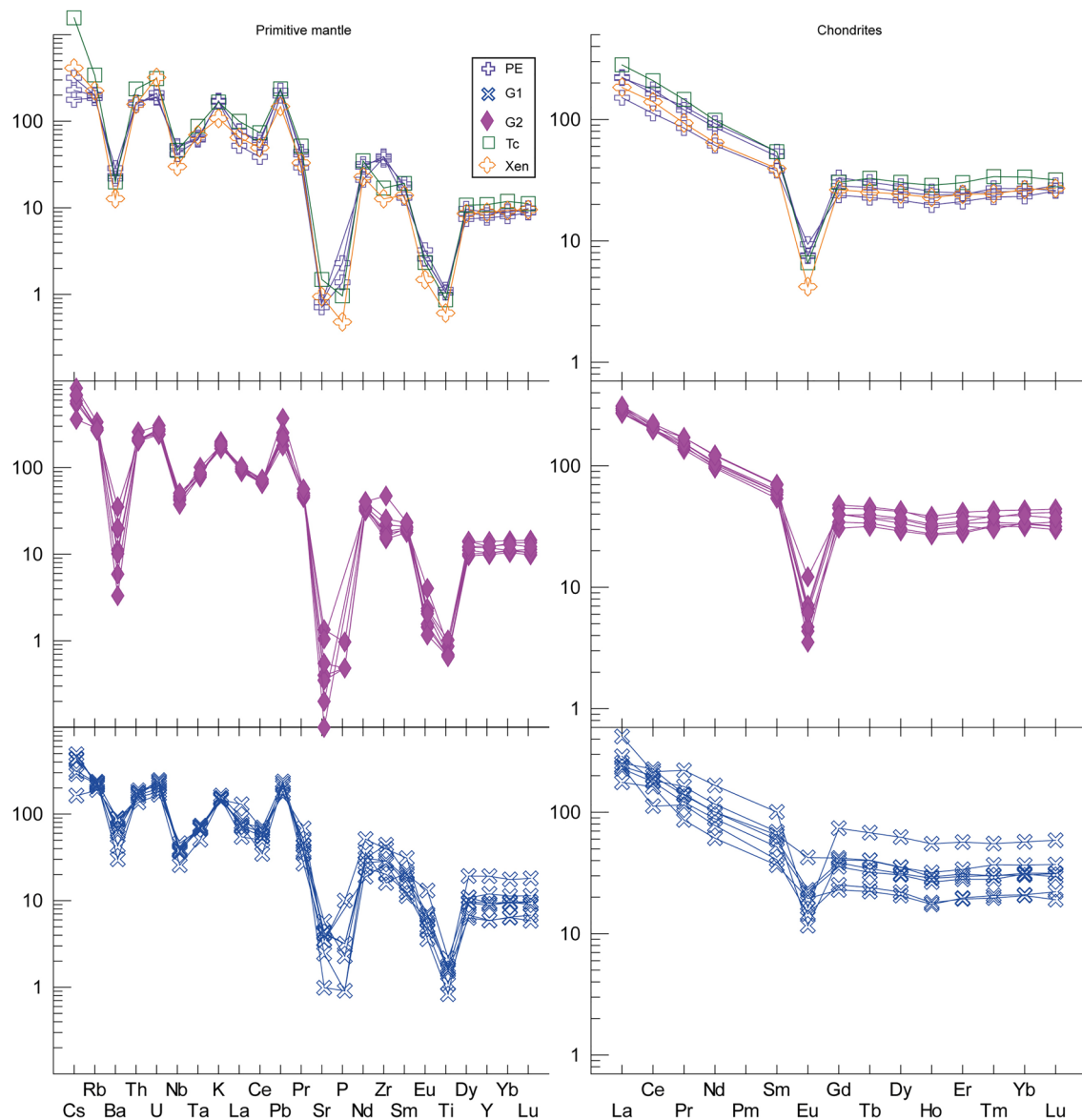
Fig. 5 Trace elements, including rare earth elements (REE), normalized to the chondrite (right) and the primitive mantle (left; Sun and McDonough 1989). Symbols as in Fig. 4. The relative enrichment of LILE (large-ion lithophile elements) when compared to the HFSE (high-field-strength elements) and the Nb–Ta–Pb anomalies reveal the calc-alkaline nature of the felsic ACC. The xenolith sample corresponds to a sample reported by Sosa-Ceballos et al. (2018). Tc compositions were obtained from Pérez-Orozco et al. (2021)

volcanic systems to have occurred during or after the depositional process.

Origin of the deposits

The PEI deposits were originally described as ignimbrites (López-Hernández et al. 2009; Avellán et al. 2019, 2020). Nonetheless, its high crystallinity (almost totally formed by crystals) and absence of pumice, ash, and low lithic contents have not been described in the literature. Given its high crystal content, we first investigate if these

deposits represent explosive, volcanic eruptions. One hypothesis that simplifies the origin of high crystallinity is that the PEI formed as part of an intrusive body that was exhumed and exposed by erosion. We think this hypothesis is unlikely because the deposits are welded at the bottom, but not the top, the deposit has a tabular shape, and there is a systematic thinning of the deposits that fill the valleys toward the east (Fig. 1b). Field evidence suggests these rocks are ignimbrites that erupted from the eastern border of the caldera, where the deposits are thicker and thin toward the northeast (López-Hernández et al. 2009;
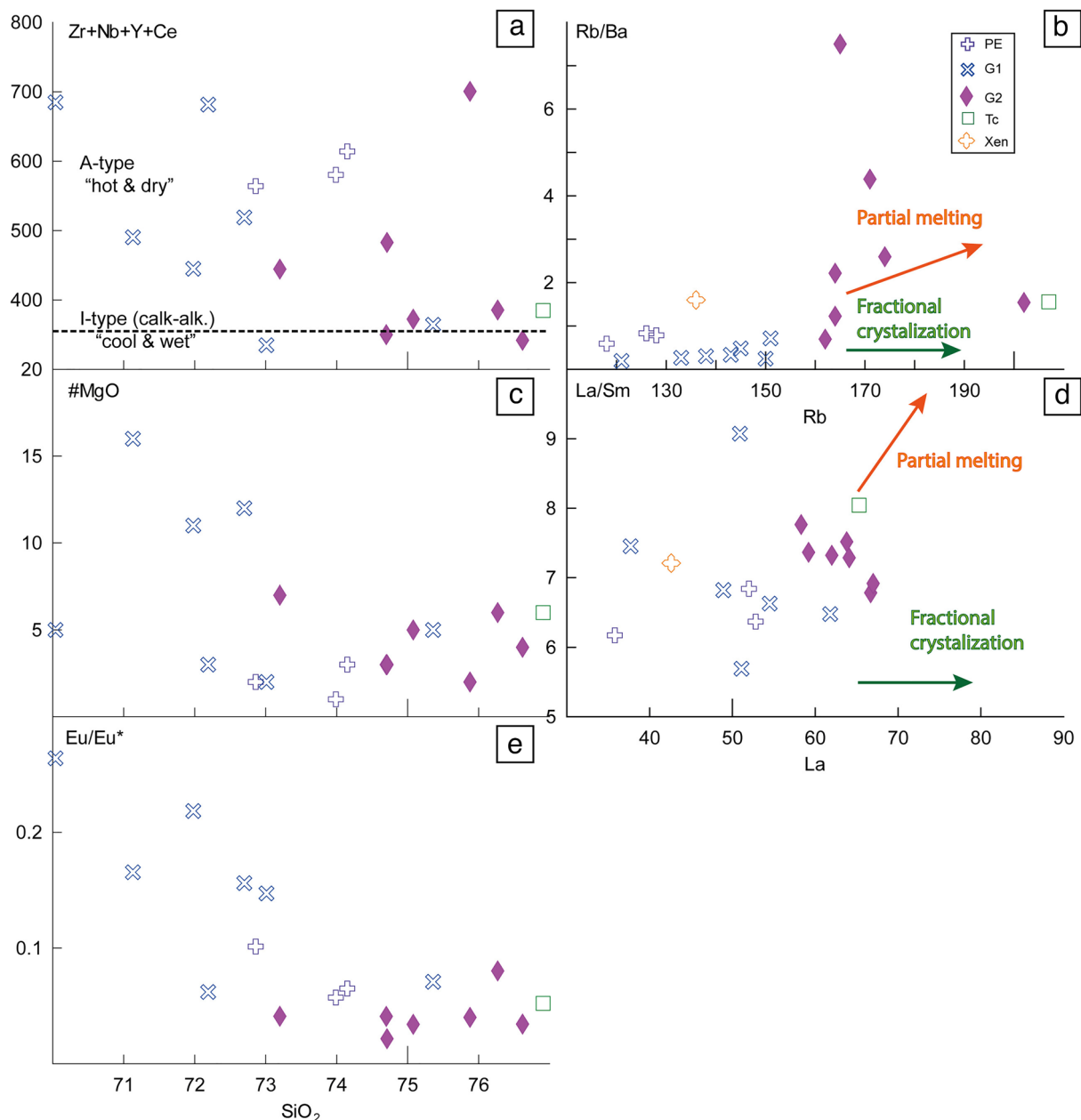
Fig. 6 **a** Zr+Nb+Y+Ce vs SiO₂ diagram of the ACC rhyolites, a dotted line separates A- from I-type rhyolites based on Whalen et al. (1987). **b** Rb/Ba vs Rb diagram displays the relation between crys- tallization vs partial melting of the ACC. **c** #Mg vs SiO₂ of the PEI rhyolites shows the low #Mg contents of the most of samples. **d** La/ Sm vs La diagram, **e** Eu/Eu* vs SiO₂ diagram. Symbols as in Fig. 4

Avellán et al. 2019). Due to hydrothermal alteration and the massive structure of the deposits (Fig. 2a, b, c), it is hard to tell if PEI was formed by the aggradation of one eruption or by multi-PDC. However, Avellán et al. (2019, 2020) describe several flow units that suggest a multi-PDC origin for the PEI. The PEI deposits are highly crystalline: the top of the deposit contains more than 70% phenocrysts with sizes ≥ 2 mm, whereas the middle and bottom portions contain up to 40–60% of phenocrysts

(Fig. 3a). Moreover, the phenocrysts are embedded in a groundmass formed exclusively by microcrysts of pol- ymorphs of silica and K-feldspar, devoid of glass. The presence of K-feldspar megacrysts suggests that the PEI magmas crystallized near its rheologic lock-up threshold, as K-feldspar phenocrystals do not precipitate signifi- cantly while they are mobile (e.g., Glazner and Johnson (2013). Arzilli et al. (2020) suggest that changes in crystal fraction of alkali feldspar can range from hours to several
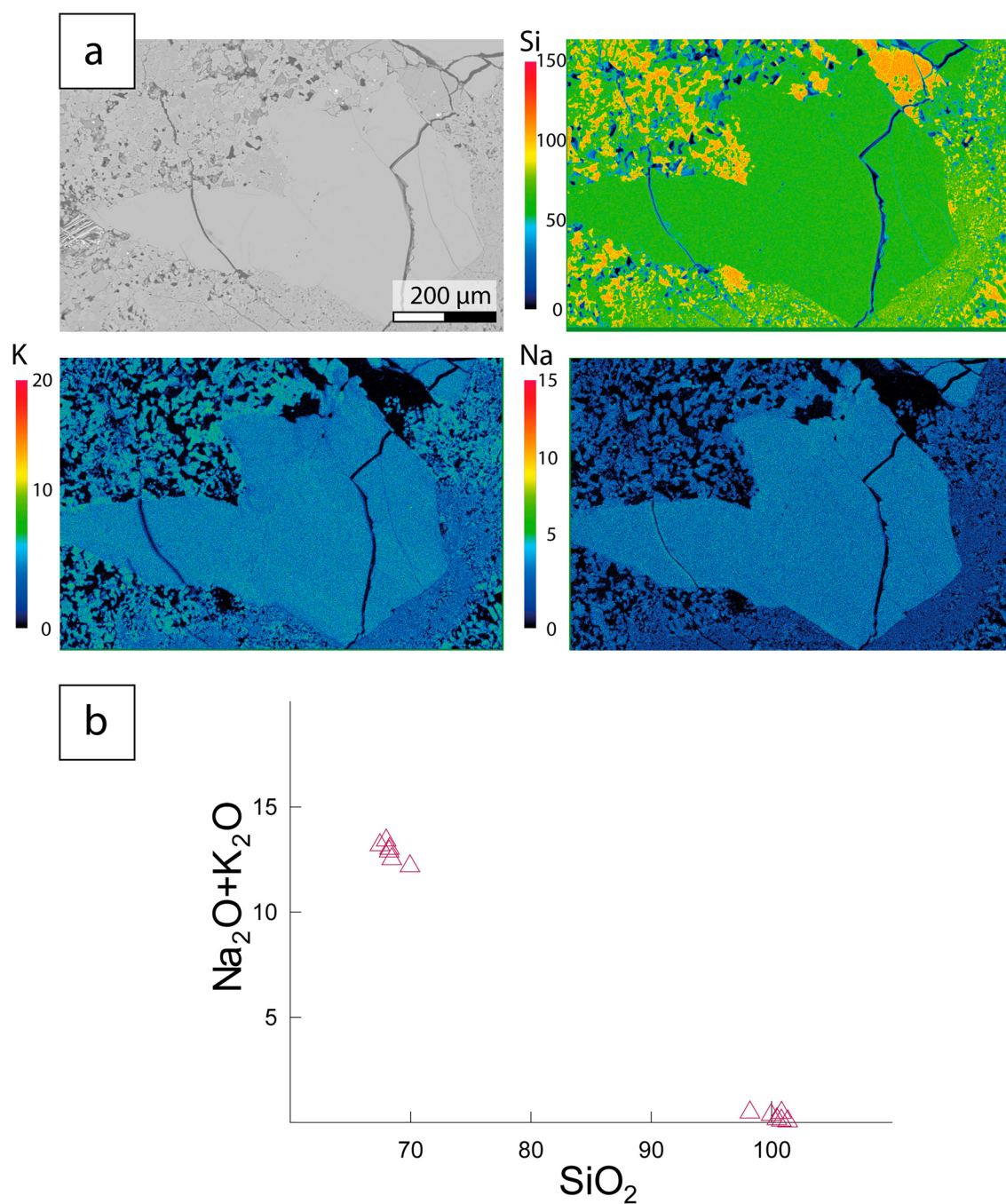
Fig. 7 Matrix composition shown as **a** X-ray maps of the matrix and feldspar. Semiquantitative X-ray maps show the homogeneous composition of the anorthoclase phenocryst and the composition of the matrix that is formed entirely of quartz polymorphs and k-feldspars. The lateral scale shows the relative concentrations of Si, K, and Na in relative intensities [arbitrary units]. **b** Total alkali vs silica diagram of the matrix made with quantitative EPMA analysis to have a compositional reference

days as a function of undercooling and H_2O content in the melt generating the alkali feldspar nucleation delay and growth. Therefore, we suggest that the low changes in Or content in the PEI phenocrysts of anorthoclases suggest large periods of storage and growth under same P–T conditions. Thus, the size and abundance of crystals (some of them with exsolution textures) and the absence of pumice strongly suggest that the PEI deposits represent a crystal mush (crystals + melt) mobilized to the surface.

Fig. 8 **a** and **b** Micrographs of ferropseudobrookite and ulvospinel crystal whit a–a´ and b–b´ transects. **c** and **d** FeO_{total} (blue line and rectangles) and TiO_2 (green line and rectangles) concentrations vs distance (µm). **e** and **f** Oxides in rutile–wustite–hematite classification diagrams. Ferropseudobrookite has a relatively consistent composition across the transect a—a'. Disequilibrium in **a** and **b** is evidenced by the rounded form and bay rims of the crystals. The compositional changes in ulvospinel tend to be more extreme than those observed in ferropseudobrookite. **g** and **h** Oxide exsolution
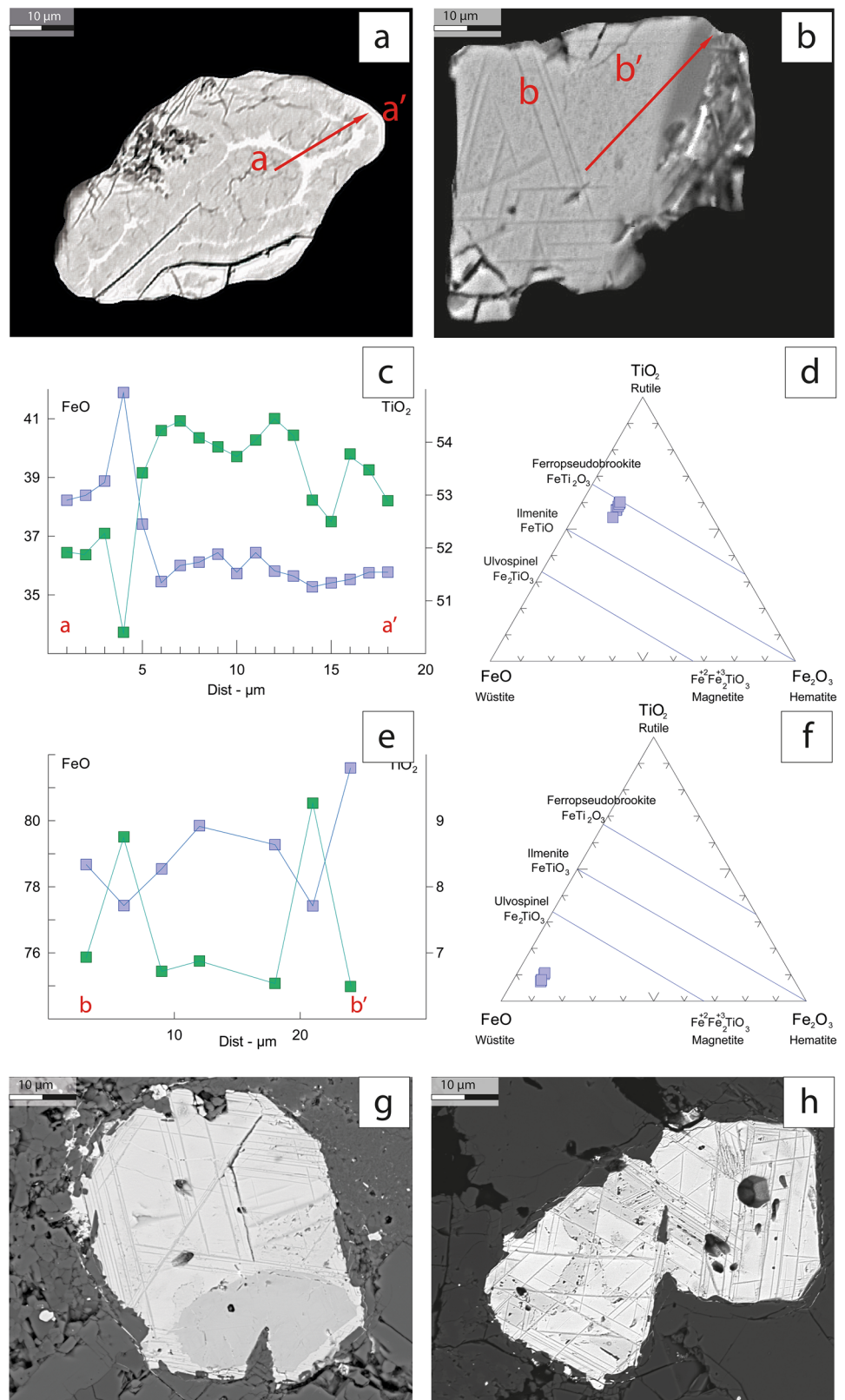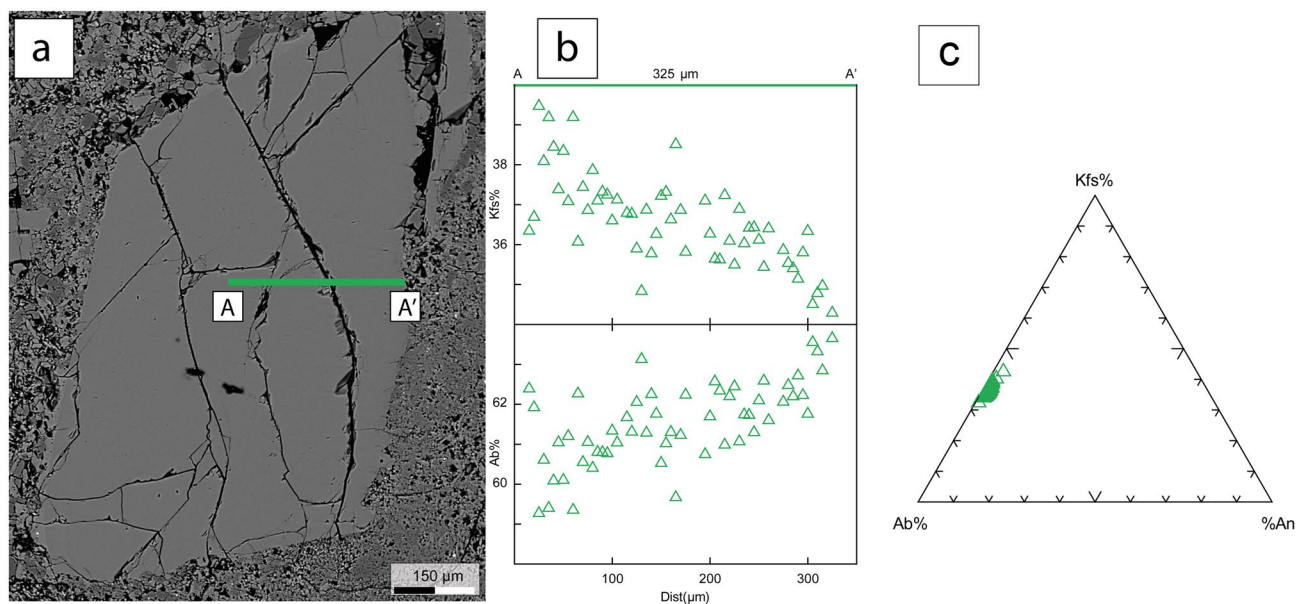
Fig. 9 Feldspar compositional transect, **a** secondary electron image of an anorthoclase crystal, **b** compositional transect (A–A') of anorthoclase. Note the slight compositional variation from center to rim where the center tends to be more potassic. c) Felspar classification diagram showing low felspar compositional variations

Fig. 10 Representative X-ray diffraction patterns of volcanic ash samples (black) with Rietveld refinement fits (grey) and background fits (red-dashed) averaged across three sample replicates. Peak positions of reference mineral phases are displayed above with the most dominant peaks outlined in black (Harlow 1982; Levien et al. 1980; Downs and Palmer 1994; Hirose et al. 2005; Lee and Xu 2019)
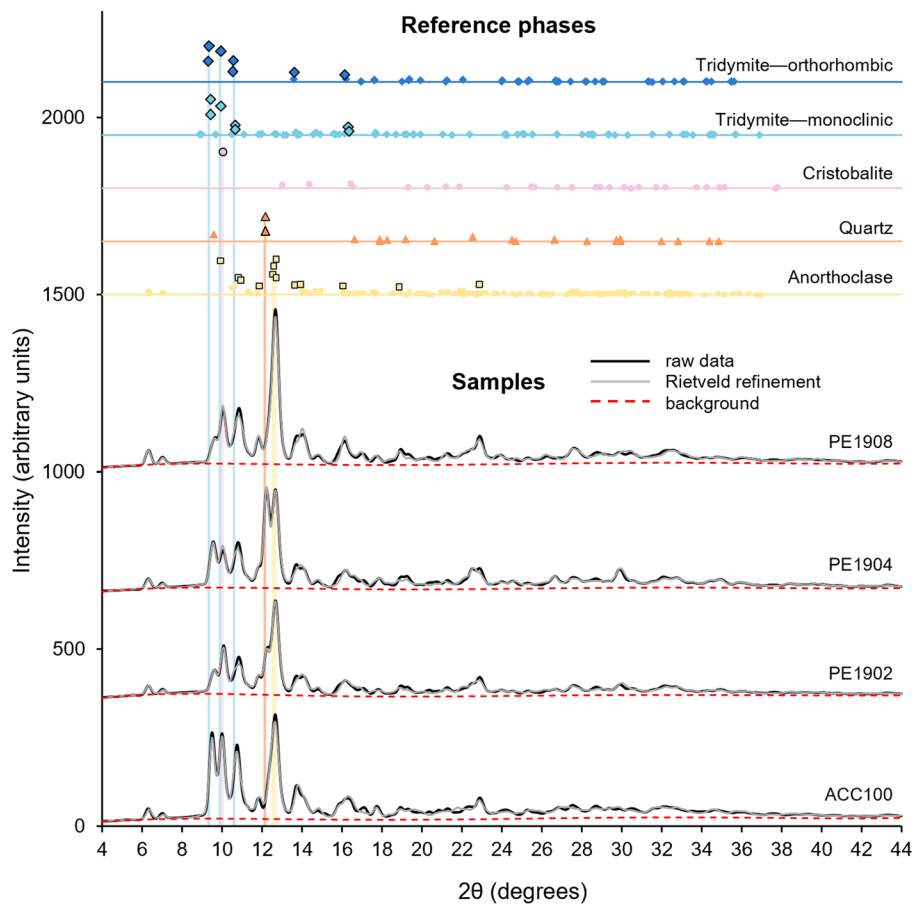
Table 2 Mineral phases determined by XRD on PEI samples

Sample	Phase	Phase %	s.d	Wt %	s.d
ACC100	Anorthoclase	51.6	0.8	63.1	1
	Quartz	16.2	3.4	4.9	0.6
	Cristobalite	9.6	2.6	2.6	0.4
	Tridymite–Monoclinic	6.2	0.5	20.3	0.9
	Tridymite–Orthorhombic	16.4	1.6	9	0.6
	Total	100		100	
PE1902	Anorthoclase	51.1	7.5	78.4	0.3
	Quartz	34.2	5.5	13	0.5
	Cristobalite	13.8	0.2	4.7	0.3
	Tridymite–Monoclinic	0.9	0.3	3.8	0.4
	Total	100		100	
PE1904	Anorthoclase	42.2	1.6	70.3	0.4
	Quartz	52	2.9	21.5	1
	Cristobalite	4.3	5.7	1.6	0.9
	Tridymite–Monoclinic	1.5	0.5	6.6	0.8
	Total	100		100	
PE1908	Anorthoclase	76	1.1	88.5	1.7
	Quartz	18.4	3.4	5.3	0.8
	Cristobalite	4	4.5	1.1	0.9
	Tridymite–Monoclinic	1.6	0.5	5.1	1.1
	Total	100		100	

Storage before eruption

Recent geological, geophysical, and petrological studies proposed a series of magma storage zones below the ACC (Sosa-Ceballos et al. 2018; Avellán et al. 2020; Pérez-Orozco et al. 2021). These storage zones match well with the depths proposed by Townsend and Huber (2020) for magma reservoirs (150–250 MPa, approximately 6–10 km) and transitory-shallow magma accumulations (< 150 MPa), although they are slightly shallower than those proposed by Gualda and Ghiorso (2013) for rhyolites with the observed silica content. Petrologic evidence including exsolution textures and phenocryst sizes (assuming that phenocryst growth occurs at depth) found in the PEI deposits support a long, protracted interval of crystallization in a plutonic body. Furthermore, ambient noise seismic tomography of the anisotropic shear wave velocities reveals mafic intrusion below the E caldera border and NW outer zone (Perton et al. 2022). Geothermal exportation wells in Acoculco reach 1900 m below the surface and intersected an intrusive body at ~ 1600 m (Yáñez-García 1980; López-Hernández et al. 2009). Aeromagnetic studies found a series of magmatic intrusive bodies hosted by calcareous rocks at depths of 1000–2500 m below the ACC (López-Hernández et al. 2009; Avellán et al. 2020). Given their location, depth, and magnetic susceptibility, these intrusions were considered to be mafic.

We suggest a series of mafic magmas intruded the local basement, creating skarns and marbles, and underplated vast zones of the ACC surrounding areas; evidence for this is the magnetic anomaly interpreted for the NE border of the ACC (Fig. 13), below the PEI deposits, and the occurrence of monogenetic-mafic volcanism along the SE–NE vicinity of the ACC.

We propose that these mafic magmas underplated the crystal-rich mush at depths of 100–250 MPa, progressively contributing to its partial melting (e.g., Sas et al. 2021; Eichelberger 2020). This eventually mobilized the mush sufficiently for the magma to erupt. Feldspar crystals in the PEI deposits contain rounded borders (Fig. 3) but are characterized by almost constant core–rim compositions (Figs. 7, 9). We propose that rim disequilibrium is produced by temperature changes during the ultimate processes that led to the eruption. Constant core–rim compositions could be produced by crystallization over a narrow range in P–T (e.g., such as might happen near the eutectic which is where we would expect to get such a high vol. fraction of crystals at constant composition), which drive melt-crystal evolution, buffered by volatile flux (e.g., Blundy et al. 2006). This process would maintain essentially constant crystal composition. Volatiles could be fluxed by magmas underplating the intrusive bodies (e.g., Huber et al. 2010; Sas et al. 2021).

The interaction of the mush with new mafic pulses and its volatiles (Fig. 12), such as that occurs across other caldera systems (i.e., Sohn et al. 2009; Watts et al. 2016; Repstock et al. 2018), could initiate mush mobilization prior to eruption; Pérez-Orozco et al. (2021) and Peiffer et al. (2014) reported anomalous high fluxing of CO_2 within the caldera perhaps as the result of mafic magmas degassing at depth. Thus, the mass transfer of volatiles from the new intrusion brings heat to the system. In consequence, this process can enhance "defrosting" and possibly could generate the subsequent remobilization of the mush to the surface (Huber et al. 2010).

Mobilization to the surface

Despite the processes of extraction and pre-eruptive storage are often treated in tandem (Bachmann and Bergantz 2004a, 2008b), it is important to separate the two processes (Gualda et al. 2019). We discuss the mobilization of PEI as a crystal-rich magma in the context of ACC and its potential transportation to the surface. The transport of crystal-rich magma from the upper crust to the surface represents a rheological and structural problem as the high magma viscosity and yield strength hinders easy transport. To address this issue, we suggest that the PEI mush had a critical melt fraction prior to eruption and, most importantly, it was in an eruptible state. The melt fraction promoted a continuum transition from a partially molten solid to a mushy liquid at about
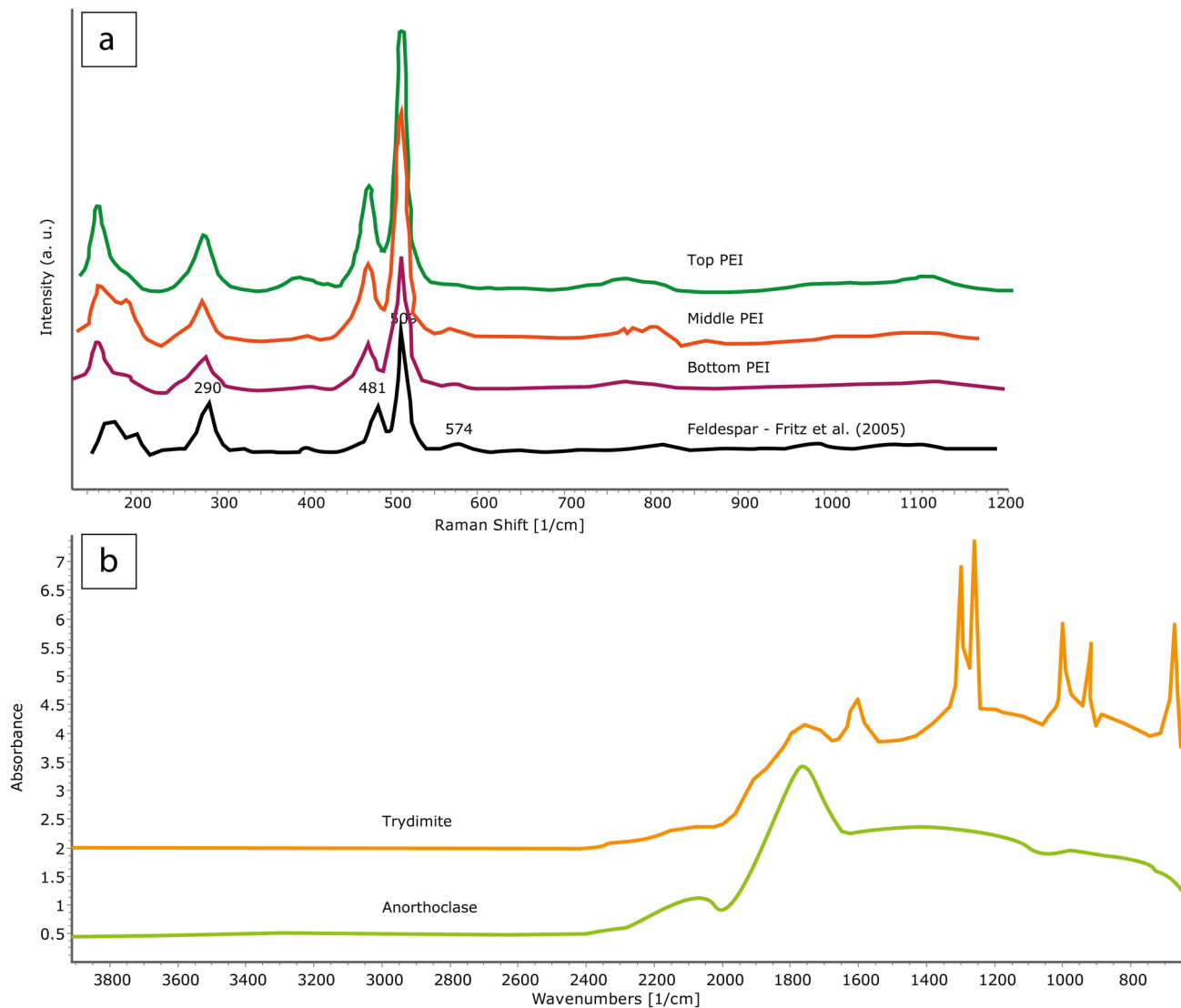
Fig. 11 **a** Raman spectra of micro-crystals surrounding phenocrysts from different stratigraphic positions, as well as, a characteristic feldspar spectrum (Fritz et al. 2005). **b** FTIR spectra of tridymite and anorthoclase crystals from the bottom of the PEI. Note that the OH–H₂O bands (3000–3800 cm⁻¹) show no structural dislocation/defects of water or hydroxyl. This could suggest the diffusion of OH–H₂O due to hydrothermal alteration

50–55 vol% crystals (e.g., (Marsh 2000). Furthermore, the bulk viscosity could change orders of magnitude between 40 and 60% crystallization (Lejeune and Richet 1995). Above the critical crystallinity of ~ 50 vol%, the crystals form a strong interlocking network that restricts flow, whereas viscosity and yield strength drop rapidly as crystallinity declines (Marsh 2000). Moreover, the transient state from Newtonian to non-Newtonian conduct occurs between 30 and 50% of crystals (Petford 2003), and the drop in the viscosity could be promoted by the recharge of hotter mafic magmas. For that reason, these critical rheological shifts arise close to the critical crystallinity for the very large volume of rhyolites described here. The lower viscosities produced through the hot magma recharges allows felsic magmas reach the surface in form of dikes, with width less than 20 m (Petford et al. 1994). These dikes are probably located both inside and outside the caldera (Fig. 1), following post-collapse faults generated during the lithospheric extensional episodes in the region (García-Palomo et al. 2002, 2018) let the magmas to infill the faults through the dike propagation (Petford et al. 1994; Weinberg 1996; Karlstrom et al. 2012; Cruden and Weinberg 2018). Dike propagation can experience a rheological transition when the eruption starts (Karlstrom et al. 2012) In the case of the PEI, we propose that extension could generate structural conditions that facilitate mafic recharge. Recharge events would
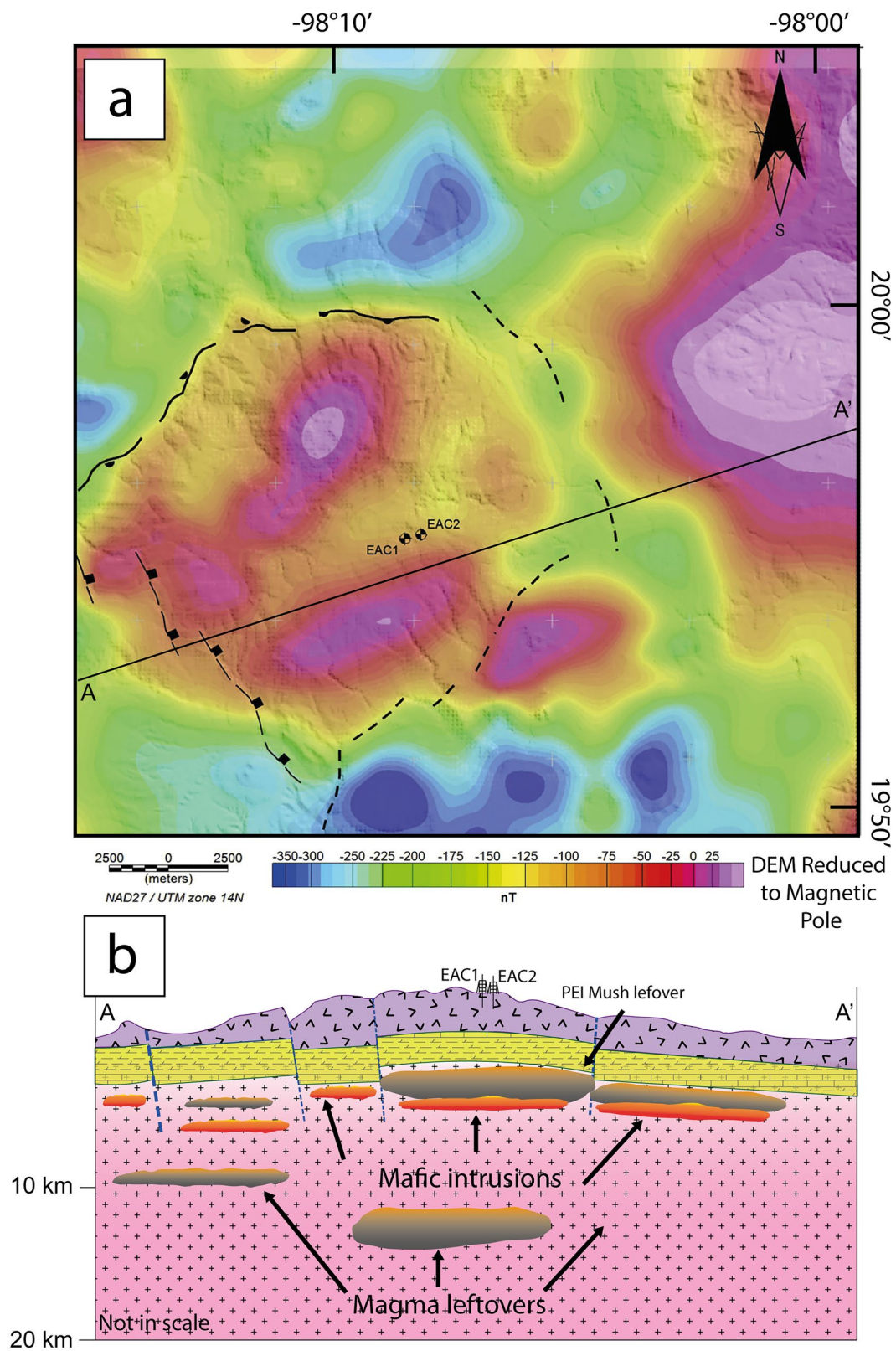
in turn decrease the PEI viscosity and yield strength, at least temporarily, and enhance the likelihood of eruption. Consequently, the PEI eruption occurred in the eastern part of the ACC, where the displacement or reactivation of a regional fault, likely the ancient caldera rim, led to the eruption. This

◄**Fig. 12 a**) Magnetic field reduced to the pole (MFRP) map of the ACC region modified from Avellan et al. (2020); EAC1 and EAC2 represent the CFE boreholes. We propose that the anomalies characterized by -25 to 25 [nT] (center and NE of the caldera) represent mafic intrusions that contributed to form the crystal mush and expulsed it to the surface; the mafic magmas not only stalled at depth, but they also formed the monogenetic volcanos on the eastern side of the caldera. **b** Simplified cross-section profile (A–A') showing the location of shallow intrusions and leftovers interpreted from the MFRP map. Given the crystal-rich nature of the PEI, we suggest that the crystal mush was very shallow and previously deformed by normal faults that facilitated the extraction to the surface

fault is associated with negative magnetic anomalies and lineaments as described by Avellán et al. (2020).

Geochemistry of the rhyolites and their relationship with the crystal mush

The relationship between crystal mushes, melts that generate crystal-rich ignimbrites, and their impact on subsequent effusive volcanism has not been studied in detail. Because of the compositional diversity of its felsic eruptive products, the ACC (Fig. 1a) is an ideal location for studying how highly silicic, viscous magmas impact upper crustal evolution (Fig. 4). Rhyolite lavas are the most common rock in the ACC (Fig. 1b). Overall, these rocks can be classified into two groups: 1) I-type, classic hydrous calc-alkaline arc rocks, and 2) A-type 'dry' rocks (Fig. 6a) that have classical subduction-related trace element anomalies such as negative anomalies of Nb and Ta, also positive Pb anomalies (Fig. 5). This classification cannot determine if a rhyolite was formed by a mush. Hence, we classified the rhyolitic lavas into two groups as a function of their trace elements: the first group (G1) shows variable Eu/Eu*, low Ba contents, and variable #Mg, and the second group (G2) shows low Eu/Eu*, variable Ba contents, and low #Mg (Fig. 6). In addition, G1 lavas have variable concentrations of Sr, P, Zr, and REE, whereas G2 lavas are less variable, although the negative anomalies shown in Ba, P, Sr, and Ti are more pronounced (Fig. 5).

G1 trace elements can be explained by events of fractional crystallization of plagioclase and ferromagnesian minerals. Whereas trace elements in G2 rocks are relatively constant and mimic the patterns and anomalies found in the PEI rocks (anomalies in Ba, Sr, P and Ti are characteristic in peralkaline rhyolites). However, we cannot neglect that some fractional crystallization occurred to form G2 rocks. Thus, rocks related to crystal mush extracts probably show features of partial melting caused by the distributed dissolution of crystals. Crystal dissolution is a process described in crystal mush systems (Bachmann et al. 2002; Deering et al. 2011; Pamukcu et al. 2013; Sliwinski et al. 2017; Szymanowski et al. 2017; Foley et al. 2020; Lubbers et al. 2020; Tavazzani et al. 2020) promoted, in general, by the injection of hot mafic magma that can lead to minimal chemical interaction and unevenly distributed
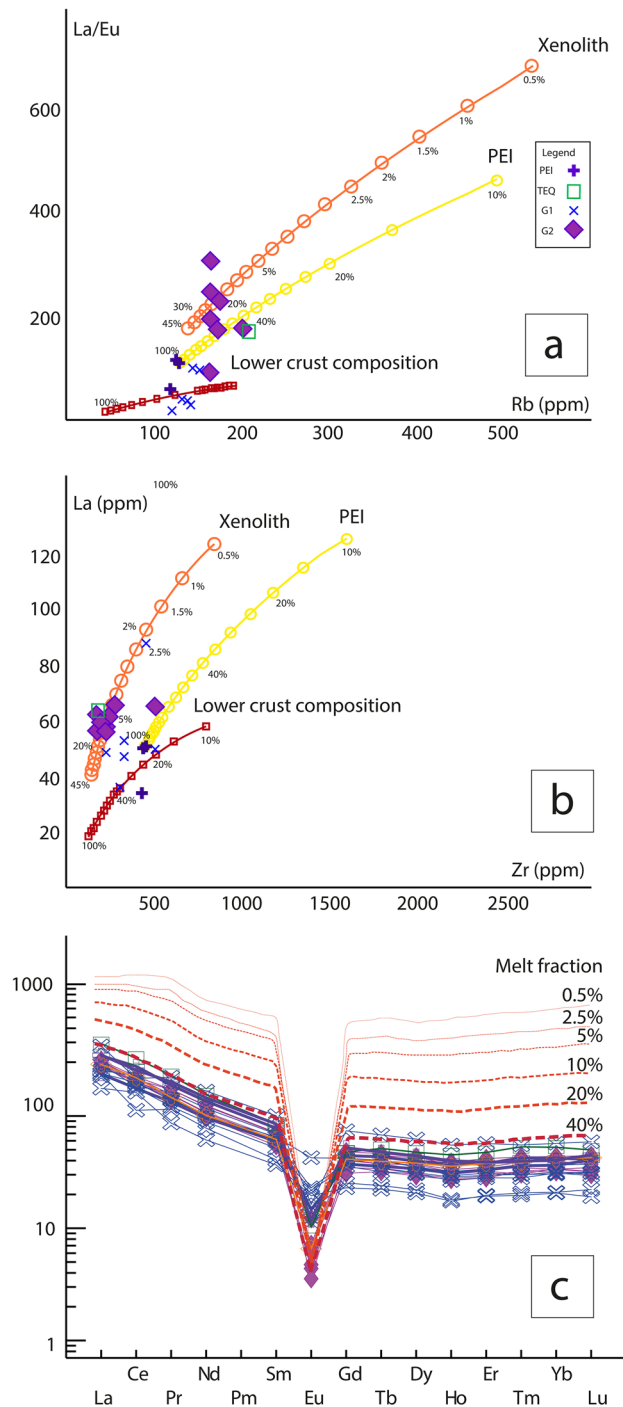
Fig. 13 Geochemical models consider diverse degrees of partial melting (0.5–40% of partial melting) of a granitic xenolith (orange lines), lower (red line), middle (light red), and upper crust (pink line) showing the behavior of ACC rhyolitic samples in **a** La/Eu vs Rb, **b** La/Zr, **c** REE concentrations

thermal flux (Foley et al. 2020). Consequently, the rocks produced by the partial melting of crystal mush will inherit certain geochemical patterns sensitive to modeling.
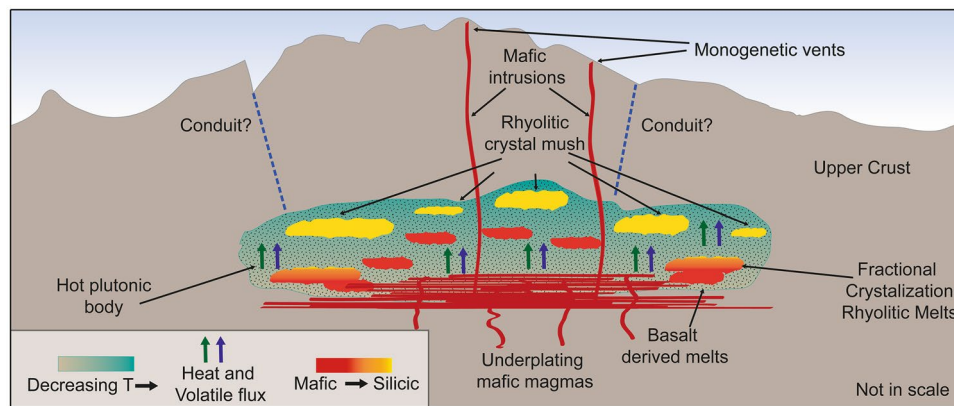
Fig. 14 Schematic model of rhyolite petrogenesis at the ACC. The generation of multiple melt compositions at the ACC is driven by fractional crystallization of subduction-related intermediate magmas and the mush extracts from A-type peralkaline intrusive bodies. The PEI represent mush (melt + crystals) mobilized to the surface, other ACC rhyolites seem to be pure melts extracted from the crystal mush and other I-type magmas. The underplating of mafic magmas drives some parts of the hot plutonic body to a crystal mush state. The thermal and volatile input also reduces density and viscosity through partial melting of mushed parts of the pluton increasing its buoyancy

As observed in G1 and G2, some rocks fit the partial melt models; G2 rocks fit better the model performed with the xenolith as end member, > 40% of partial melting (Fig. 13), whereas G1, as seen in the model using PEI as end member, could represent relatively high degrees of PEI partial melting (Fig. 13). Although G1 and G2 overall fit the models, we cannot exclude the possibility that multiple crystal mushes serve as magma sources; idealizing such models suffer well-recognized limitations: lack of samples, uncertainty about the composition abundance of comprising phases and subsurface alteration. Hence, given the differences shown by G1 and G2 rocks, our best approximation is to suggest that rhyolites in the ACC were produced by at least two different sources, one of which could be related to the partial melting of the rocks remobilized to be deposited as the PEI.

Rhyolite formation model

We propose a model for rhyolite formation in the ACC (Fig. 14). Primary melts are formed in a subduction zone for the TMVB (e.g., Gómez-Tuena et al. (2018); Parolari et al. (2021). The G1 rhyolites were formed by fractional crystallization of intermediate magmas, probably of tholeiitic-transitional compositions that arrived at the upper crust and assimilated some country rock (e.g., Sosa-Ceballos et al. 2021). Given the distance from the trench ~ 450 km, the crustal thickness ~ 40 km, and the depth of the slab below the ACC ~ 300 km (Pérez-Campos et al. 2008; Ferrari et al. 2012; Castellanos et al. 2018), some melts formed A-type peralkaline intrusive bodies in a back-arc type environment (e.g., Karsli et al. 2012; Jiang et al. 2006). Perhaps, the influence of the mantle flow in this region, produced by the rollback and slab tear of the Cocos plate (Castellanos et al. 2018), generated the tectonic extension that promoted the ascent of the melts

in this part of the TMVB. Thus, mafic magmas that erupted through monogenetic vents around the ACC, but these features are equally or even more common in western TMVB, served as the heating element melting the intrusive body, forming the crystal mush and the G2 rhyolites. Melting and extracting the crystal mush dispersed the pyroclastic density currents that emplaced the PEI deposits at the surface.

Conclusion

The ultra-crystalline rhyolitic PEI was erupted ~ 1.2 Ma ago through the eastern portion of the ACC. The PEI is composed primarily of compositionally homogeneous K-felspar and quartz polymorphs. The high crystallinity (close to ~ 100%) in the PEI is the result of two independent main processes: magmatic crystallization and hydrothermal recrystallization of the matrix. Protracted crystallization at shallow depths produced up to the 50% of crystals and post-depositional hydrothermal alteration causes devitrification of the remaining matrix to produce cristobalite + tridymite crystals. The presence of this ultra-crystal-rich rhyolitic ign-imbrites in ACC suggests that some felsic eruptions are the product of the remobilization of a crystalline mush. Injection or recharge of hot magma resulted in the transport of the mush and its extracts from the crust to the surface. We suggest that the mafic magmas that erupted through monogenetic vents around the ACC served as the heating element that promoted the partial melting and mobilization of underplate intrusive bodies. Thus, the geochemical diversity of the ACC rhyolites reflects a complex combination of different magmatic processes. The ACC rhyolites can be divided into G1 ("I-type") calkaline and G2 ("A-type") peralkaline. We suggest that most of the G1 and G2 rhyolites

could represent relatively high degrees of partial melting and were produced by at least two different sources, one of which could be related to melt extracts of the crystal mush in which PEI magma were formed.

References

Anderson AT, Davis AM, Lu F (2000) Evolution of Bishop Tuff Rhyolitic Magma Based on Melt and Magnetite Inclusions and Zoned Phenocrysts. J Petrol 41:449–473. https://doi.org/10.1093/PETROLOGY/41.3.449

Antao SM, Hassan I, Wang J et al (2008) State-of-the-art high-resolution powder x-ray diffraction (HRPXRD) illustrated with Rietveld structure refinement of quartz, sodalite, tremolite, and meionite. Can Mineral 46:1501–1509. https://doi.org/10.3749/CANMIN.46.5.1501

Arzilli F, Stabile P, Fabbrizio A et al (2020) Crystallization Kinetics of Alkali Feldspar in Peralkaline Rhyolitic Melts: Implications for Pantelleria Volcano. Front Earth Sci (lausanne). https://doi.org/10.3389/FEART.2020.00177/BIBTEX

Avellán DR, Macías JL, Layer PW et al (2019) Geology of the late Pliocene-Pleistocene Acoculco caldera complex, eastern Trans-Mexican Volcanic Belt (México). J Maps 15:8–18

Avellán DR, Macías JL, Layer PW et al (2020) Eruptive chronology of the Acoculco caldera complex: A resurgent caldera in the eastern Trans-Mexican Volcanic Belt (México). J South Am Earth Sci. https://doi.org/10.1016/J.JSAMES.2019.102412

Bachmann O, Bergantz GW (2003) Rejuvenation of the Fish Canyon magma body: A window into the evolution of large-volume silicic magma systems. Geology 31:789–792. https://doi.org/10.1130/G19764.1

Bachmann O, Bergantz GW (2004a) On the origin of crystal-poor rhyolites: extracted from batholithic crystal mushes. J Petrol 45:1565–1582

Bachmann O, Bergantz G (2008a) The Magma Reservoirs That Feed Supereruptions. Elements 4:17–21. https://doi.org/10.2113/GSELEMENTS.4.1.17

Bachmann O, Bergantz GW (2008b) Rhyolites and their Source Mushes across Tectonic Settings. J Petrol 49:2277–2285. https://doi.org/10.1093/PETROLOGY/EGN068

Bachmann O, Dungan MA, Lipman PW (2002) The Fish Canyon Magma Body, San Juan Volcanic Field, Colorado: Rejuvenation and Eruption of an Upper-Crustal Batholith. J Petrol 43:1469–1503. https://doi.org/10.1093/PETROLOGY/43.8.1469

Bindeman I (2008) Oxygen Isotopes in Mantle and Crustal Magmas as Revealed by Single Crystal Analysis. Rev Mineral Geochem 69:445–478. https://doi.org/10.2138/RMG.2008.69.12

Bindeman IN, Valley JW (2003) Rapid generation of both high- and low-$\delta18O$, large-volume silicic magmas at the Timber Mountain/Oasis Valley caldera complex, Nevada. GSA Bull 115:581–595. https://doi.org/10.1130/0016-7606(2003)115%3c0581:RGOBHA%3e2.0.CO;2

Blundy J, Cashman K (2008) Petrologic Reconstruction of Magmatic System Variables and Processes. Rev Mineral Geochem 69:179–239. https://doi.org/10.2138/RMG.2008.69.6

Blundy J, Cashman K, Humphreys M (2006) Magma heating by decompression-driven crystallization beneath andesite volcanoes. Nature 443:76–80

Brophy JG (1991) Composition gaps, critical crystallinity, and fractional crystallization in orogenic (calc-alkaline) magmatic systems. Contrib Miner Petrol 109:173–182. https://doi.org/10.1007/BF00306477/METRICS

Browne PRL (1978) Hydrothermal alteration in active geothermal fields. Annu Rev Earth Planet Sci 6:229–248

Calcagno P, Trumpy E, Gutiérrez-Negrín LC, Norini G, Macías JA, Carrasco-Núñez G, Liotta D, Garduño-Monroy VH, Hersir GP, Vaessen L, Evanno G (2019) Updating the 3D Geomodels of Los Humeros and Acoculco Geothermal Systems (Mexico)-H2020 GEMex Project

Canet C, Hernández-Cruz B, Jiménez-Franco A et al (2015) Combining ammonium mapping and short-wave infrared (SWIR) reflectance spectroscopy to constrain a model of hydrothermal alteration for the Acoculco geothermal zone, Eastern Mexico. Geothermics 53:154–165. https://doi.org/10.1016/J.GEOTHERMICS.2014.05.012

Capaccioni B, Coniglio S (1995) Varicolored and vesiculated tuffs from La Fossa volcano, Vulcano Island (Aeolian Archipelago, Italy): evidence of syndepositional alteration processes. Bull Volcanol 57:61–70. https://doi.org/10.1007/BF00298708/METRICS

Cashman KV, Giordano G (2014) Calderas and magma reservoirs. J Volcanol Geoth Res 288:28–45. https://doi.org/10.1016/J.JVOLGEORES.2014.09.007

Cashman KV, Sparks RSJ, Blundy JD (2017) Vertically extensive and unstable magmatic systems: A unified view of igneous processes. Science. https://doi.org/10.1126/SCIENCE.AAG3055

Castellanos JC, Clayton RW, Pérez-Campos X (2018) Imaging the Eastern Trans-Mexican Volcanic Belt With Ambient Seismic Noise: Evidence for a Slab Tear. J Geophys Res Solid Earth 123:7741–7759. https://doi.org/10.1029/2018JB015783

Clemens JD, Bryan SE, Mayne MJ et al (2022) How are silicic volcanic and plutonic systems related? Part 1: A review of geological and geophysical observations, and insights from igneous rock chemistry. Earth Sci Rev. https://doi.org/10.1016/J.EARSCIREV.2022.104249

Crovisier JL, Honnorez J, Fritz B, Petit JC (1992) Dissolution of sub-glacial volcanic glasses from Iceland: laboratory study and modelling. Appl Geochem 7:55–81. https://doi.org/10.1016/S0883-2927(09)80064-4

Cruden AR, Weinberg RF (2018) Mechanisms of Magma Transport and Storage in the Lower and Middle Crust—Magma Segregation, Ascent and Emplacement. In: Steffi Burchardt (ed) Volcanic and igneous plumbing systems 13–53. https://doi.org/10.1016/B978-0-12-809749-6.00002-9

Deer WA, Howie RA, Wise WS, Zussman J (2004) Framework silicates : silica minerals, feldspathoids and the zeolites. In: Rock-forming minerals, vol 4B, 2nd edn. The Geological Society, London, pp 493–523

Deering CD, Bachmann O, Vogel TA (2011) The Ammonia Tanks Tuff: Erupting a melt-rich rhyolite cap and its remobilized crystal cumulate. Earth Planet Sci Lett 310:518–525. https://doi.org/10.1016/J.EPSL.2011.08.032

Downs RT, Palmer DC (1994) The pressure behavior of c cristobalite. American Mineralogisl 79:9–14

Eichelberger J (2020) Distribution and Transport of Thermal Energy within Magma–Hydrothermal Systems. Geosciences 212(10):212. https://doi.org/10.3390/GEOSCIENCES10060212

Engvik AKP, Gerald AF, John D, Austrheim H (2008) Albitization of granitic rocks: the mechanism of replacement of oligoclase by albite. Can Mineral 46:1401–1415. https://doi.org/10.3749/canmin.46.6.1401

Ferrari L, Orozco-Esquivel T, Manea V, Manea M (2012) The dynamic history of the Trans-Mexican Volcanic Belt and the Mexico subduction zone. Tectonophysics 522:122–149

Foley ML, Miller CF, Gualda GAR (2020) Architecture of a Super-sized Magma Chamber and Remobilization of its Basal Cumulate (Peach Spring Tuff, USA) P E T R O L O G Y. J Petrol 61:20. https://doi.org/10.1093/petrology/egaa020

Fritz J, Greshake A, Stöffler D (2005) Micro-Raman spectroscopy of plagioclase and maskelynite in Martian meteorites: Evidence of progressive shock metamorphism. Antarct Meteor Res 18:96

Furnes H (1978) Element mobility during palagonitization of a subglacial hyaloclastite in Iceland. Chem Geol 22:249–264. https://doi.org/10.1016/0009-2541(78)90034-7

García-Palomo A, Macías JL, Tolson G et al (2002) Volcanic stratigraphy and geological evolution of the Apan region, east-central sector of the Trans-Mexican Volcanic Belt. Geofísica Internacional 41:133–150

García-Palomo A, Macías JL, Jiménez A et al (2018) NW-SE Pliocene-Quaternary extension in the Apan-Acoculco region, eastern Trans-Mexican Volcanic Belt. J Volcanol Geoth Res 349:240–255. https://doi.org/10.1016/J.JVOLGEORES.2017.11.005

Giggenbach WF (1984) Mass transfer in hydrothermal alteration systems—A conceptual approach. Geochim Cosmochim Acta 48:2693–2711. https://doi.org/10.1016/0016-7037(84)90317-X

Giordano G, Caricchi L (2022) Determining the state of activity of transcrustal magmatic systems and their volcanoes. Ann Rev Earth Planet Sci 50:231-259. https://doi.org/10.1146/ANNUREV-EARTH-032320-084733

Glazner AF, Johnson BR (2013) Late crystallization of K-feldspar and the paradox of megacrystic granites. Contrib Miner Petrol 166:777–799. https://doi.org/10.1007/S00410-013-0914-1/FIGURES/16

Gómez-Alvarez F, Garduño-Monroy VH, Sosa-Ceballos G et al (2021) New constraints on tectonism and magmatism from the eastern sector of the Trans-Mexican Volcanic Belt (Chignahuapan Horst. J South Am Earth Sci, Puebla, México). https://doi.org/10.1016/J.JSAMES.2021.103468

Gómez-Tuena A, Mori L, Straub SM (2018) Geochemical and petrological insights into the tectonic origin of the Transmexican Volcanic Belt. Earth Sci Rev 183:153–181. https://doi.org/10.1016/J.EARSCIREV.2016.12.006

Gottsmann J, Lavallée Y, Martí J, Aguirre-Díaz G (2009) Magma–tectonic interaction and the eruption of silicic batholiths. Earth Planet Sci Lett 284:426–434. https://doi.org/10.1016/J.EPSL.2009.05.008

Gualda GAR, Ghiorso MS (2013) Geological note low-pressure origin of high-silica rhyolites and granites. J Geol 121:537–545. https://doi.org/10.1086/671395/ASSET/IMAGES/LARGE/FG4_ONLINE.JPEG

Gualda GAR, Gravley DM, Deering CD, Ghiorso MS (2019) Magma extraction pressures and the architecture of volcanic plumbing systems. Earth Planet Sci Lett 522:118–124. https://doi.org/10.1016/J.EPSL.2019.06.020

Harlow GE (1982) The anorthoclase structures: the effects of temperature and composition. Am Miner 67:975–996

Hay RL, Iijima A (1968) Nature and Origin of Palagonite Tuffs of the Honolulu Group on Oahu. Haw Mem Geol Soc Am 116:331–376. https://doi.org/10.1130/MEM116-P331

Heaney PJ, Veblen DR, Post JE (1994) Structural disparities between chalcedony and macrocrystalline quartz. Am Miner 79:452–460

Hildreth W (1981) Gradients in silicic magma chambers: Implications for lithospheric magmatism. J Geophys Res Solid Earth 86:10153–10192. https://doi.org/10.1029/JB086IB11P10153

Hildreth W, Wilson CJN (2007) Compositional Zoning of the Bishop Tuff. J Petrol 48:951–999. https://doi.org/10.1093/PETROLOGY/EGM007

Hirose T, Kihara K, Okuno M et al (2005) X-ray, DTA and Raman studies of monoclinic tridymite and its higher temperature orthorhombic modification with varying temperature. J Mineral Petrol Sci 100:55

Huber C, Bachmann O, Manga M (2010) Two Competing Effects of Volatiles on Heat Transfer in Crystal-rich Magmas: Thermal Insulation vs Defrosting. J Petrol 51:847–867. https://doi.org/10.1093/PETROLOGY/EGQ003

Ibrahim K, Hall A (1996) The authigenic zeolites of the Aritayn Volcaniclastic Formation, north-east Jordan. Miner Depos 31:514–522. https://doi.org/10.1007/BF00196131/METRICS

Jiang YH, Jiang SY, Zhao KD, Ling HF (2006) Petrogenesis of Late Jurassic Qianlishan granites and mafic dykes, Southeast China: implications for a back-arc extension setting. Geol Mag 143:457–474. https://doi.org/10.1017/S0016756805001652

Jolles JSR, Lange RA (2021) Origin of Compositional Gradients with Temperature in the High-SiO2 Rhyolite Portion of the Bishop Tuff: Constraints on Mineral–Melt–Fluid Reactions in the Parental Mush. J Petrol 62:1–25. https://doi.org/10.1093/PETROLOGY/EGAB087

Karlstrom L, Rudolph ML, Manga M (2012) Caldera size modulated by the yield stress within a crystal-rich magma reservoir. Nat Geosci. https://doi.org/10.1038/ngeo1453

Karsli O, Caran Ş, Dokuz A et al (2012) A-type granitoids from the Eastern Pontides, NE Turkey: Records for generation of hybrid A-type rocks in a subduction-related environment. Tectonophysics 530–531:208–224. https://doi.org/10.1016/J.TECTO.2011.12.030

Kihara K, Matsumoto T, Imamura M (1986) Structural change of orthorhombic-I tridymite with temperature: A study based on second-order thermal-vibrational parameters. Z Kristallogr Cryst Mater 177:27–38. https://doi.org/10.1524/ZKRI.1986.177.14.27

Kimball KL (1990) Effects of hydrothermal alteration on the compositions of chromian spinels. Contrib Miner Petrol 105:337–346. https://doi.org/10.1007/BF00306543/METRICS

Kousehlar M, Weisenberger TB, Tutti F, Mirnejad H (2012) Fluid control on low-temperature mineral formation in volcanic rocks of Kahrizak. Iran Geofluids 12:295–311. https://doi.org/10.1111/GFL.12001

Lee S, Xu H (2019) Using powder XRD and pair distribution function to determine anisotropic atomic displacement parameters of orthorhombic tridymite and tetragonal cristobalite. Acta Crystallogr B Struct Sci Cryst Eng Mater 75:160–167. https://doi.org/10.1107/S2052520619000933/DK5075SUP4.PDF

Lejeune AM, Richet P (1995) Rheology of crystal-bearing silicate melts: An experimental study at high viscosities. J Geophys Res Solid Earth 100:4215–4229. https://doi.org/10.1029/94JB02985

Levien L, Prewitt CT, Weidner DJ (1980) Structure and elastic properties of quartz at pressure. Am Mineral 65(9-10):920–930

López-Hernández A, García-Estrada G, Aguirre-Díaz G et al (2009) Hydrothermal activity in the Tulancingo-Acoculco Caldera Complex, central Mexico: Exploratory studies. Geothermics 38:279–293. https://doi.org/10.1016/J.GEOTHERMICS.2009.05.001

Lopez-Hernandez A, Castillo-Hernandez D (1997) Exploratory drilling at Acoculco, Puebla, Mexico: A hydrothermal system with only nonthermal manifestations (Conference) | OSTI.GOV. https://www.osti.gov/biblio/602731

Lubbers J, Deering C, Bachmann O (2020) Genesis of rhyolitic melts in the upper crust: Fractionation and remobilization of an intermediate cumulate at Lake City caldera. J Volcanol Geother Res, Colorado, USA. https://doi.org/10.1016/J.JVOLGEORES.2019.106750

Macías JL, Sheridan MF, Espíndola JM (1997) Reappraisal of the 1982 eruptions of El Chichón Volcano, Chiapas, Mexico: New data from proximal deposits. Bull Volcanol 58:459–471. https://doi.org/10.1007/S004450050155/METRICS

Malfait WJ, Seifert R, Petitgirard S et al (2014) Supervolcano eruptions driven by melt buoyancy in large silicic magma chambers. Nat Geosci. https://doi.org/10.1038/ngeo2042

Marsh BD (1981) On the crystallinity, probability of occurrence, and rheology of lava and magma. Contrib Miner Petrol 78:85–98. https://doi.org/10.1007/BF00371146/METRICS

Marsh BD (2000) Reservoirs of magma and magma chambers. In: Sigurdsson H (ed) Encyclopedia of volcanoes. Academic, vol 1607. pp 191–206

Mathieu L (2018) Quantifying Hydrothermal Alteration: A Review of Methods. Geosciences 245(8):245. https://doi.org/10.3390/GEOSCIENCES8070245

Nadoll P, Mauk JL (2011) Wüstite in a hydrothermal silver-lead-zinc vein, Lucky Friday mine, Coeur d'Alene mining district, U.S.A. Am Miner 96:261–267. https://doi.org/10.2138/AM.2011.3553/MACHINEREADABLECITATION/RIS

Pamukcu AS, Carley TL, Gualda GAR et al (2013) The Evolution of the Peach Spring Giant Magma Body: Evidence from Accessory Mineral Textures and Compositions, Bulk Pumice and Glass Geochemistry, and Rhyolite-MELTS Modeling. J Petrol 54:1109–1148. https://doi.org/10.1093/PETROLOGY/EGT007

Pandarinath K, García-Soto AY, Santoyo E et al (2020) Mineralogical and geochemical changes due to hydrothermal alteration of the volcanic rocks at Acoculco geothermal system, Mexico. Geol J 55:6508–6526. https://doi.org/10.1002/GJ.3817

Pardo M, Suarez G (1995) Shape of the subducted Rivera and Cocos plates in southern Mexico: Seismic and tectonic implications. J Geophys Res Solid Earth 100:12357–12373. https://doi.org/10.1029/95JB00919

Parolari M, Gómez-Tuena A, Errázuriz-Henao C, Cavazos-Tovar JG (2021) Orogenic andesites and their link to the continental rock cycle. Lithos. https://doi.org/10.1016/J.LITHOS.2020.105958

Pauly BD, Schiffman P, Zierenberg RA et al (2011) Environmental and chemical controls on palagonitization. Geochem Geophys Geosyst 12:12017. https://doi.org/10.1029/2011GC003639

Peiffer L, Bernard-Romero R, Mazot A et al (2014) Fluid geochemistry and soil gas fluxes (CO2–CH4–H2S) at a promissory Hot Dry Rock Geothermal System: The Acoculco caldera, Mexico. J Volcanol Geoth Res 284:122–137. https://doi.org/10.1016/J.JVOLGEORES.2014.07.019

Pérez-Campos X, Kim YH, Husker A et al (2008) Horizontal subduction and truncation of the Cocos Plate beneath central Mexico. Geophys Res Lett. https://doi.org/10.1029/2008GL035127

Pérez-Orozco JD, Sosa-Ceballos G, Macías JL (2021) Tectonic and magmatic controls on the evolution of post-collapse volcanism. Lithos, Insights from the Acoculco Caldera Complex, Puebla, México. https://doi.org/10.1016/J.LITHOS.2020.105878

Perton M, Maldonado Hernández LT, Figueroa-Soto A et al (2022) The magmatic plumbing system of the Acoculco volcanic complex (Mexico) revealed by ambient noise tomography. J Volcanol Geother Res. https://doi.org/10.1016/J.JVOLGEORES.2022.107704

Petford N, Lister JR, Kerr RC (1994) The ascent of felsic magmas in dykes. Lithos 32:161–168. https://doi.org/10.1016/0024-4937(94)90028-0

Petford N (2003) Rheology of Granitic Magmas During Ascent and Emplacement. Ann Rev Earth Planet Sci 31(1):399–427

Post JE, Bish DL (1989) Rietveld refinement of crystal structures using powder X-ray diffraction data. Mod Powder Diffr 20:277–30

Repstock A, Breitkreuz C, Lapp M, Schulz B (2018) Voluminous and crystal-rich igneous rocks of the Permian Wurzen volcanic system, northern Saxony, Germany: physical volcanology and geochemical characterization. Int J Earth Sci 107:1485–1513. https://doi.org/10.1007/S00531-017-1554-X/FIGURES/14

Rollinson HR (2014) Using Geochemical Data: Evaluation. Using Geochemical Data, Presentation, Interpretation. https://doi.org/10.4324/9781315845548

Rowe MC, Ellis BS, Lindeberg A (2012) Quantifying crystallization and devitrification of rhyolites by means of X-ray diffraction and electron microprobe analysis. Am Miner 97:1685–1699. https://doi.org/10.2138/AM.2012.4006

Sánchez-Córdova MM, Canet C, Rodríguez-Díaz A et al (2020) Water-rock interactions in the Acoculco geothermal system, eastern Mexico: Insights from paragenesis and elemental mass-balance. Geochemistry. https://doi.org/10.1016/J.CHEMER.2019.06.003

Sas M, Shane P, Kuritani T et al (2021) Mush, Melts and Metasediments: a History of Rhyolites from the Okataina Volcanic Centre, New Zealand, as Captured in Plagioclase. J Petrol 62:1–26. https://doi.org/10.1093/PETROLOGY/EGAB038

Scaillet B, Holtz F, Pichavant M (2016) Experimental Constraints on the Formation of Silicic Magmas. Elements 12:109–114. https://doi.org/10.2113/GSELEMENTS.12.2.109

Schwartz GM (1959) Hydrothermal alteration. Econ Geol 54:161–183. https://doi.org/10.2113/GSECONGEO.54.2.161

Seifert W, Thomas R, Rhede D et al (2010) Origin of coexisting wüstite, Mg–Fe and REE phosphate minerals in graphite-bearing fluorapatite from the Rumburk granite. Eur J Mineral 22:495–507. https://doi.org/10.1127/0935-1221/2010/0022-2034

Sliwinski JT, Bachmann O, Dungan MA et al (2017) Rapid pre-eruptive thermal rejuvenation in a large silicic magma body: the case of the Masonic Park Tuff, Southern Rocky Mountain volcanic field, CO, USA. Contrib Miner Petrol 172:1–20. https://doi.org/10.1007/S00410-017-1351-3/FIGURES/9

Sohn YK, Son M, Jeong JO, Jeon YM (2009) Eruption and emplacement of a laterally extensive, crystal-rich, and pumice-free ignimbrite (the Cretaceous Kusandong Tuff, Korea). Sediment Geol 220:190–203. https://doi.org/10.1016/J.SEDGEO.2009.04.020

Sosa-Ceballos G, Macías JL, Avellán DR et al (2018) The Acoculco Caldera Complex magmas: Genesis, evolution and relation with the Acoculco geothermal system. J Volcanol Geoth Res 358:288–306. https://doi.org/10.1016/J.JVOLGEORES.2018.06.002

Sosa-Ceballos G, Boijseauneau-López ME, Perez-Orozco JD et al (2021) Silicic magmas in the Michoacan-Guanajuato volcanic

field: An overview of plumbing systems, crustal storage, and genetic processes. Rev Mex Cienc Geol 38:210–225

Stroncik NA, Schmincke HU (2001) Evolution of palagonite: Crystallization, chemical changes, and element budget. GeochemGeophy Geosyst. https://doi.org/10.1029/2000GC000102

Sun SS, McDonough WF (1989) Chemical and isotopic systematics of oceanic basalts: Implications for mantle composition and processes. Geol Soc Spec Publ 42:313–345. https://doi.org/10.1144/GSL.SP.1989.042.01.19

Szymanowski D, Wotzlaw JF, Ellis BS et al (2017) Protracted near-solidus storage and pre-eruptive rejuvenation of large magma reservoirs. Nat Geosci. https://doi.org/10.1038/ngeo3020

Tavazzani L, Peres S, Sinigoi S et al (2020) Timescales and Mechanisms of Crystal-mush Rejuvenation and Melt Extraction Recorded in Permian Plutonic and Volcanic Rocks of the Sesia Magmatic System (Southern Alps, Italy). J Petrol 61:49. https://doi.org/10.1093/PETROLOGY/EGAA049

Toby BH, Von Dreele RB (2013) GSAS-II: the genesis of a modern open-source all purpose crystallography software package. J Appl Crystallogr 46(2):544–549. https://doi.org/10.1107/S0021889813003531

Townsend M, Huber C (2020) A critical magma chamber size for volcanic eruptions. Geology 48:431–435. https://doi.org/10.1130/G47045.1

Troch J, Huber C, Bachmann O (2022) The physical and chemical evolution of magmatic fluids in near-solidus silicic magma reservoirs: Implications for the formation of pegmatites. Am Miner 107:190–205. https://doi.org/10.2138/AM-2021-7915/ASSET/GRAPHIC/J_AM-2021-7915_FIG_004.JPG

Vigneresse JL, Barbey P, Cuney M (1996) Rheological transitions during partial melting and crystallization with application to felsic magma segregation and transfer. J Petrol 37:1579–1600. https://doi.org/10.1093/PETROLOGY/37.6.1579

Walton AW, Schiffman P, Walton AW, Schiffman P (2003) Alteration of hyaloclastites in the HSDP 2 Phase 1 Drill Core 1. Description and paragenesis. Geochem Geophys Geosys. https://doi.org/10.1029/2002GC000368

Watts KE, John DA, Colgan JP et al (2016) Probing the Volcanic-Plutonic Connection and the Genesis of Crystal-rich Rhyolite in a Deeply Dissected Supervolcano in the Nevada Great Basin: Source of the Late Eocene Caetano Tuff. J Petrol 57:1599–1644. https://doi.org/10.1093/PETROLOGY/EGW051

Weinberg RF (1996) Ascent mechanism of felsic magmas: news and views. Earth Environ Sci Trans R Soc Edinb 87:95–103. https://doi.org/10.1017/S0263593300006519

Whalen JB, Currie KL, Chappell BW (1987) A-type granites: geochemical characteristics, discrimination and petrogenesis. Contrib Miner Petrol 95:407–419

Whitney JA, Naldrett AJ, Robertson JM (1989) Origin and Evolution of Silicic Magmas. Ore Dep Ass Magmas. https://doi.org/10.5382/REV.04.11.k,

Yáñez-García C (1980) Informe geológico del proyecto geotérmico Los Humeros-Las Derrumbadas, estados de Puebla y Veracruz. CFE-GPG Int Rep 01:80

Zhang JH, Yang JH, Chen JY et al (2018) Genesis of late Early Cretaceous high-silica rhyolites in eastern Zhejiang Province, southeast China: A crystal mush origin with mantle input. Lithos 296–299:482–495. https://doi.org/10.1016/J.LITHOS.2017.11.026

Zhou Z, Fyfe WS (1989) Palagonitiz tion of basaltic glass from DSDP Site 335, Leg 37: Textures, chemical composition, and mechanism of formation. Am Miner 74:1045–1053